

Magnetospheric solitary structure maintained by 3000 km/s ions as a cause of westward moving auroral bulge at 19 MLT

M. Yamauchi¹, I. Dandouras^{2,*}, P. W. Daly³, G. Stenberg⁴, H. U. Frey⁵, P.-A. Lindqvist⁶, Y. Ebihara⁷, H. Nilsson¹, R. Lundin¹, H. Rème^{2,*}, M. André⁴, E. A. Kronberg³, A. Balogh⁸, and M. Henderson⁹

¹IRF, Kiruna, Sweden

²CESR, Université de Toulouse, Toulouse, France

³MPS, Katlenburg-Lindau, Germany

⁴IRF, Uppsala, Sweden

⁵UCB/SSL, Berkeley, CA, USA

⁶Alfven Lab., KTH, Stockholm, Sweden

⁷IAR, Nagoya U., Nagoya, Japan

⁸Blackett Lab., ICL, London, UK

⁹LANL, Los Alamos, NM, USA

* also at: CNRS, UMR 5187, Toulouse, France

Received: 23 April 2009 – Accepted: 20 July 2009 – Published: 27 July 2009

Abstract. In the evening equatorial magnetosphere at about $4 R_E$ geocentric distance and 19 MLT, the four Cluster spacecraft observed a solitary structure with a width of about 1000–2000 km in the propagation direction. The solitary structure propagates sunward with about 5–10 km/s carrying sunward electric field (in the propagation direction) of up to about 10 mV/m (total potential drop of about 5–10 kV), depletion of magnetic field of about 25%, and a duskward $E \times B$ convection up to 50 km/s of He⁺ rich cold plasma without O⁺. At the same time, auroral images from the IMAGE satellite together with ground based geomagnetic field data showed a westward (sunward at this location) propagating auroral bulge at the magnetically conjugate ionosphere with the solitary structure. The solitary structure is maintained by flux enhancement of selectively 3000 km/s ions (about 50 keV for H⁺, 200 keV for He⁺, and 750 keV for O⁺). These ions are the main carrier of the diamagnetic current causing the magnetic depletion, whereas the polarization is maintained by different behavior of energetic ions and electrons. Corresponding to aurora, field-aligned accelerated ionospheric plasma of several keV appeared at Cluster from both hemispheres simultaneously. Together with good correspondence in location and propagation velocity between the auroral bulge and the solitary structure, this indicates that the sunward moving auroral bulge is caused by the sunward

propagation of the solitary structure which is maintained by energetic ions. The solitary structure might also be the cause of Pi2-like magnetic variation that started simultaneously at Cluster location.

Keywords. Magnetospheric physics (Auroral phenomena; Electric fields; Energetic particles, trapped)

1 Introduction

One of the essential elements of the magnetospheric substorms is the sudden formation of a large-scale auroral bulge in the nightside ionosphere and its westward surge as well as poleward expansion (Akasofu et al., 1965). The bulge has complicated large-scale electric field and large-scale current systems (e.g. Akasofu, 1977; Iijima and Potemra, 1976; Inhester et al., 1981), and is directly related to auroral kilometric radiation and Pi2 pulsation (Benediktov et al., 1968; Gurnett et al., 1974; Rostoker, 1967; Saito et al., 1976; Olson, 1999; Morioka et al., 2009). Magnetospheric substorms also accompany sudden flux increases of energetic particles ($10^{2\sim 3}$ keV ions in the pre-midnight and $10^{1\sim 2}$ keV electrons in the post-midnight) at the nightside geosynchronous distance (Arnoldy and Chan, 1969; Reeves et al., 1990).

To understand the substorm, it is important to understand the relationship between these accompanying elements. This requires studies of the magnetospheric signatures of the ionospheric phenomena and vice versa. Among those, the



Correspondence to: M. Yamauchi
(m.yamauchi@irf.se)

magnetospheric signature of westward propagating auroral bulge in the evening sector has not been studied much compared to the other magnetospheric signature of the substorm except Roux et al. (1991). Most of the past observations of the westward moving auroral bulge in the evening sector (Oppenorth et al., 1989; Lyons et al., 1990; Fujii et al., 1994; Weimer et al., 1994; Sanchez et al., 1996; Gjerloev et al., 2007) are limited to low altitudes and not near the equatorial plane. Inversely, most of the magnetospheric observation of the auroral bulge is limited to midnight sectors where phenomena is convoluted by many effects such as Harang discontinuity (e.g., Lyons et al., 2005).

Thus, there is a missing link between the equatorial signature (ring current ions and electrons, ionospheric ions, plasmaspheric ions, DC field, wave) and the evening auroral bulge that is away from the substorm onset region. In the model, the westward motion of evening aurora has been considered as the result either by ionospheric Hall current and conductivity gradient in the magnetosphere-ionosphere coupled electromagnetic system (Kan and Sun, 1985; Lyons et al., 1990), or result of magnetic drift (summation of gradient-B drift and curvature drift) of plasma sheet ions (Vasyliunas, 1970; Wolf, 1970). The magnetosphere plays relatively a passive role in the former models, whereas the magnetospheric drift plays active role in the latter models.

Another relatively unexplored element is possible role of the flux enhancement of the energetic particles of the ring current. Several mechanisms have been proposed in the past for how the energetic ions is supplied to the ring current during magnetic storms (e.g., Williams, 1985), and substorm-related process is one of the most important candidates because of large variation in DC electric field (e.g., Akasofu and Chapmann, 1961; Williams, 1987; Kamide et al., 1998; Reeves and Henderson, 2001; Reeves et al., 2003; Daglis, 2006). However, no solid observational work has performed to understand the influence of this enhance flux to the other phenomena such as electric field and magnetic deviation.

We found an ideal event to investigate the above two topics from Cluster perigee traversal. On 19 May 2002 at around 06:43 UT, westward moving auroral bulge in the northern ionosphere observed by IMAGE/FUV arrived at conjugate location of Cluster spacecraft (SC) which were all located near the equatorial plane in the evening sector ($X = -1.2 R_E$, $Y = -4.2 R_E$, $Z = -0.4 R_E$ in Geocentric Solar-Ecliptic (GSE) coordinate, or about 19 magnetic local time (MLT) and $L = 4.4$) near its perigee. In this event, both energetic ion flux and DC electric and magnetic fields suddenly changed simultaneously when an evening auroral bulge arrived at the Cluster conjugate.

The event reported here gives information on propagation of large DC electric field in the equatorial plane; behavior of medium-energy ring current ions that is related to the DC field changes and auroral bulge; and composition of cold plasma that indicates plasmasphere expansion in the inner magnetosphere. At 19 MLT, westward direction is nearly the

same as the sunward direction. Since the Cluster data is given in the Cartesian coordinate, we use the term “sunward” when the direction matters in the Cluster data, whereas we use the traditional term “westward” for the auroral phenomena in the ionosphere. Similarly, “duskward” direction in the Cluster data corresponds to “poleward” direction in the ionospheric data.

2 Event and instrument

2.1 Event identification

Figure 1 shows Cluster particle data (RAPID in Fig. 1a and CIS in Fig. 1b and c, see Sect. 2.3 for the instrumentation) during Cluster perigee traversal (06:10~07:40 UT) on 19 May 2002. There are two epochs of sudden changes in the ion data. One is at around 06:43:00 UT in the energetic component (10~1000 keV) and the low energy component (<100 eV), and the other is at around 06:48:30 UT in the sub-keV component with some changes in the energetic component. These two events have different characteristics in the changes (energy, pitch angles, and amount of flux) and ground auroral signatures (auroral bulge and poleward leaped arc), and the relation between these two epochs is not clear. Therefore, we concentrate on the first epoch at around 06:43 UT in this paper. The second event after 06:48:30 UT is to be reported in the future.

2.2 Cluster constellation

Figure 2 shows the Cluster locations in GSE coordinate at the time of the event during the Cluster perigee traversals on 19 May 2002. The spacecraft (SC) separation is very small (70~300 km). The traversal direction is mainly northward for all spacecraft following very similar trajectories in the order of SC-1, SC-4, SC-2, and SC-3, with about 1 min lag between SC-1 and SC-4. This time lag is much longer than inter-spacecraft time lag of the phenomena, and therefore, the time lag due to satellite velocity can be ignored.

2.3 Instrument

During this event, hot electron (PEACE) instrument was switched off, but other particle instruments (CIS and RAPID) were in operation, as well as instruments for the electric and magnetic fields (EFW, FGM, STAFF), and the electron density (WHISPER). Details of these instruments are found in Rème et al. (2001) for CIS; Wilken et al. (2001) for RAPID, Gustafsson et al. (2001) for EFW; Balogh et al. (2001) for FGM; Cornilleau-Wehrin et al. (1997) for STAFF; and Decreau et al. (2001) for WHISPER.

We primarily use data from CIS and RAPID. CIS consists of two instruments for positive ions measurement at energies about few eV to tens keV for normal mode: HIA (0.004~40 keV) without mass analyzer, and CODIF

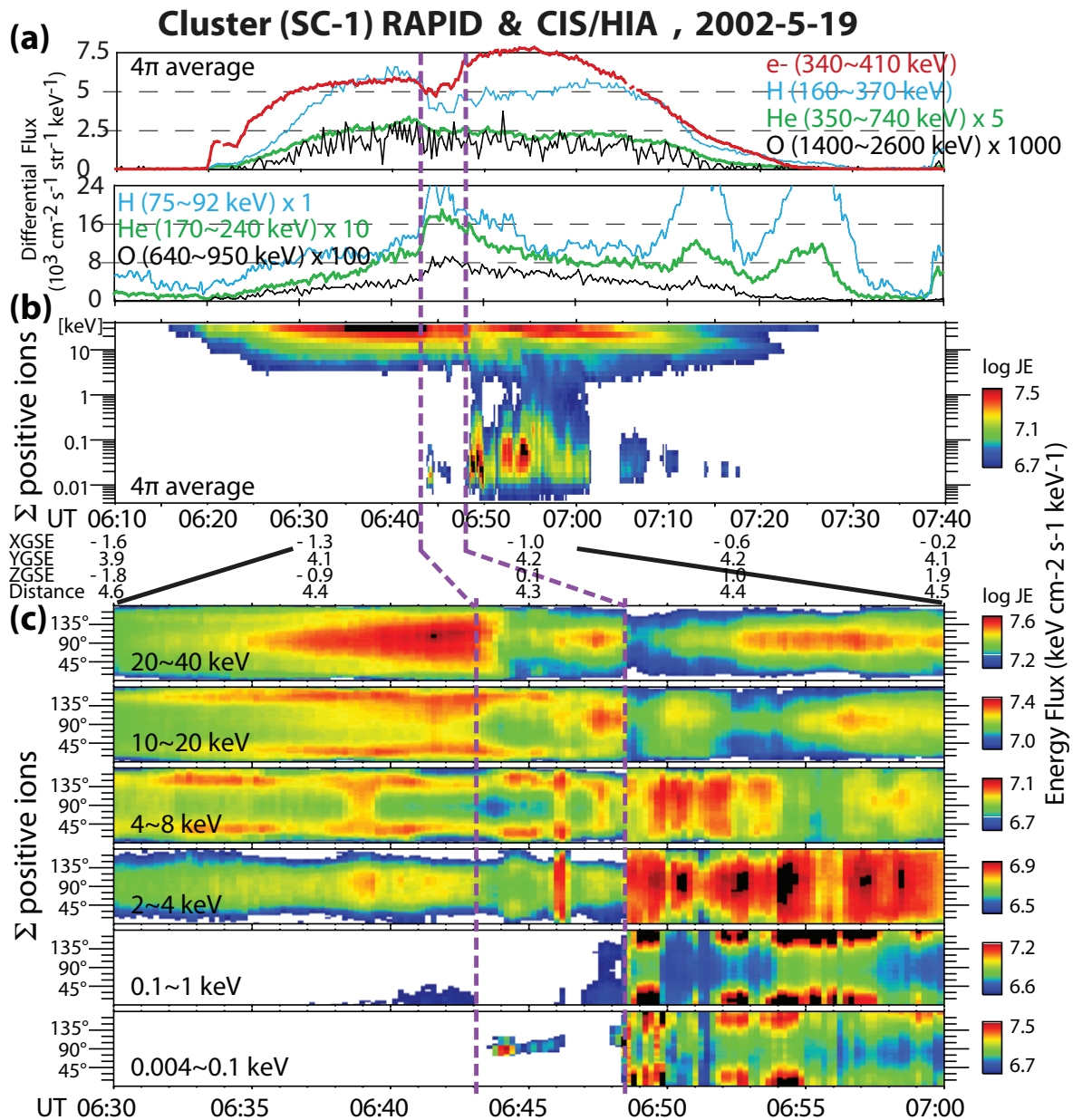


Fig. 1. Cluster particle data from spacecraft-1 during perigee traversal on 19 May 2002 during 06:10~07:40 UT. **(a)** Time series plots of 4π averaged differential fluxes ($\text{cm}^{-2} \text{s}^{-1} \text{str}^{-1} \text{keV}^{-1}$) of energetic particles observed by RAPID. Several energy channels with the same change (sudden decrease or sudden increase) at around 06:43 UT are integrated. **(b)** Energy-time spectrogram of 4π averaged differential energy flux ($\text{keV cm}^{-2} \text{s}^{-1} \text{str}^{-1} \text{keV}^{-1}$) observed by CIS/HIA. **(c)** Pitch angle-time spectrograms of differential energy fluxes observed by CIS/HIA at different energy ranges (energy-averaged). For (b) and (c), one pixel corresponds to 12 s with 4 s sampling (and averaged) and 8 s idle.

(0.03~40 keV) with mass analyzer. During this event, HIA was operational in SC-1 and SC-3 with relatively low sampling rate (a 12-s cycle of sampling one spin (4 s) and idle two spins) from only 8 sectors instead of 16 sectors, and CODIF was operational in SC-1, SC-3, and SC-4 with slightly higher sampling rate than HIA (mostly 8-s cycle of sampling one spin and idle one spin).

RAPID consists of two instruments, one for positive ions with 12 sectors at tens keV to MeV range (IIMS) and one for electrons with 9 sectors (IES) at 20~400 keV. During this event, both IIMS and IES were operational at all spacecraft with one-spin (4 s) sampling cycle for electrons and protons (H^+), and four-spin (16 s) sampling cycle for He group and CNO group. For electrons, the observation mode for SC-1

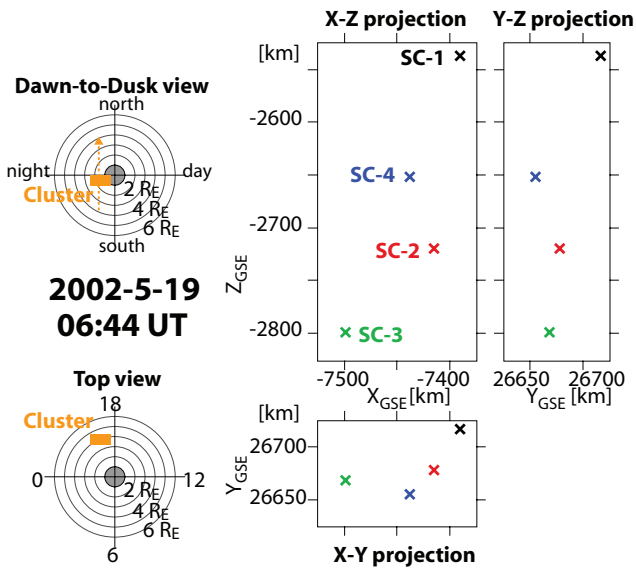


Fig. 2. Location of Cluster at 06:44 UT on 19 May 2002 in Geocentric Solar-Ecliptic (GSE) coordinate. All spacecraft are nearly at $X = -1.2 R_E$, $Y = -4.2 R_E$, $Z = -0.4 R_E$ in GSE, or about 19 MLT and $L = 4.4$. The right side shows spacecraft (SC) constellation (SC-1: black cross, SC-2: red cross, SC-3: green cross, and SC-4: blue cross). The upper panels show the $X - Z$ projection (left) and the $Y - Z$ projection (right), and the lower panel shows the $X - Y$ projection.

was not appropriate until 06:48 UT for the observed high flux, while the other spacecraft registered correct electron flux during entire period (the observation mode is switched for high flux after 06:32 UT). Fortunately, energetic component (>240 keV) is not effected by the different observation modes very much, and hence we showed this component in Fig. 1.

In addition to Cluster, we used IMAGE/FUV data (Mende et al., 2000) for auroral image, geomagnetic indices (Dst and SYM-H) for ring current development, AE (provisional AU and provisional AL from 11 stations) for substorm activity, and ASY for supplement to AE (<http://swdcwww.kugi.kyoto-u.ac.jp/wdc/Sec3.html>), ground geomagnetic data from relevant stations for conjugate check, ACE data for solar wind monitoring (<http://www.srl.caltech.edu/ACE/ASC/level2/index.html>), GOES-8 geosynchronous satellite data for the confirmation of the substorm activity, and Los Alamos National Laboratory (LANL) geosynchronous satellite for the general energetic particle data in the evening inner magnetosphere (http://leadbelly.lanl.gov/lanl_ep_data/). Explanation of SYM and ASY is found in Iyemori et al. (2009).

3 Observation

The event took place about 10 h after the arrival of interplanetary coronal mass ejection at around 20 UT (initial Dst spike of $+28$ nT) with solar wind density about 50 cm^{-3} (from 7 cm^{-3}), velocity about 500 km/s (from 350 km/s), interplanetary magnetic field (IMF) intensity about 20 nT (from 5 nT). By one hour before the event, they decreased to about 10 cm^{-3} , 430 km/s (i.e., 3 nPa), and 15 nT. The solar wind and geomagnetic activities are thus high but not extreme. In fact this interplanetary coronal mass ejection caused only a minor magnetic storm with minimum $D_{st} = -58$ nT at 06~07 UT and minimum SYM-H = -71 nT at 07:09~07:11 UT. These values indicate minor level of ring current development (Iyemori et al., 2009). The composition of the ring current (H^+ flux dominate over O^+ flux) also confirms that this is a minor storm (e.g., Daglis, 2006).

3.1 Geomagnetic and optical condition

Before the SYM-H minimum at 07:10 UT, SYM-H continuously decreased from the sudden commencement 10 h before (starting from about $+60$ nT). During latest 3 h, SYM-H monotonically decreased except for a short recovery during 06:28~06:36 UT. Embedded in this ring current development, a substorm expansion is recognized at around 06:26~06:34 UT in the geomagnetic field data, and the short recovery of SYM-H mentioned above is due to the substorm-related disruption of the cross-tail current (Ohtani et al., 2001).

Figure 3 shows AL and AU indices, and geomagnetic deviations (X-component, relative values) from Macquarie Island (MCQ), Sitka (SIT), and Meanook (MEA) during 06:20~06:50 UT (1 min resolution). MCQ is the nearest conjugate of Cluster (only 5° off in magnetic longitude and 1° off in magnetic latitude). Starting at around 06:25 UT, AL decreased during 06:25~06:33 UT. This corresponds to a substorm expansion in the midnight sector as observed by IMAGE.

Figure 4 shows the IMAGE/FUV data (Mende et al., 2000) during 06:23~06:46 UT (2 min resolution). It shows a brightening of an auroral arc (onset of a substorm) at midnight at around 06:25 UT with subsequent expansion of the auroral bulge during the next several minutes. Geostationary GOES-8 satellite at around 01 LT also detected dipolarization at around 06:26 UT (not shown here). The MEA station in Fig. 3 corresponds to the westward edge of this substorm auroral bulge after 06:30 UT.

During this expansion, the brightest region of the midnight auroral bulge is limited to only 5° in latitude in the post-midnight sector and less than 3° in latitude in the pre-midnight sector, whereas a less intense auroral arc (indicated by a dashed arrow) poleward of this auroral bulge in the pre-midnight sector is intensified without moving its position. The pre-midnight bulge part stayed equatorward of this

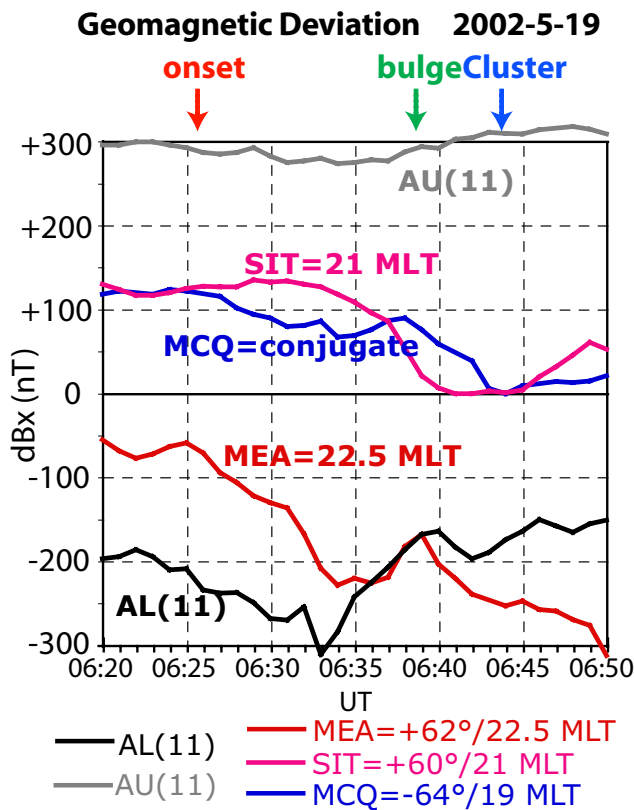


Fig. 3. The provisional AU and AL indices from 11 stations and geomagnetic deviation X-component from three stations during 06:20~06:50 UT on 19 May 2002. The numbers given after each station's code at the bottoms are the corrected geomagnetic latitude and the magnetic local time. Note that the corrected geomagnetic latitude is sometimes different from the dipole geomagnetic latitude by up to 4° (MCQ is -60° in the dipole coordinate). MCQ is also the nearest conjugate of Cluster (only 5° off in magnetic longitude and 1° off in magnetic latitude) during this period. The timings of “onset” and “bulge” in the figure are determined by IMAGE/FUV auroral image in Fig. 4, and the event “Cluster” is the time when Cluster detected large change in Fig. 1.

poleward arc, i.e., stayed far inside the separatrix. Thus, this bulge belongs to the type reported by Murphree and Cogger (1992), and is not the type proposed by Lyons et al. (1990) or Ober et al. (2001). The double-arc structure is seen in the entire evening sector, one at around 60° geomagnetic latitude (GMLat), and another at 70°~75°GMLat.

Both the AL index and the IMAGE/FUV image show short duration of this substorm (less than 10 min). The decrease of AL stopped at 06:33 UT with only 100 nT change from the substorm onset, and AL started to recover already from 06:34 UT. The midnight auroral brightening stopped at around 06:34 UT for both equatorward bulge and poleward arc, and they substantially faded by 06:42 UT. The quick decay is also found in the mid latitudes where the decay

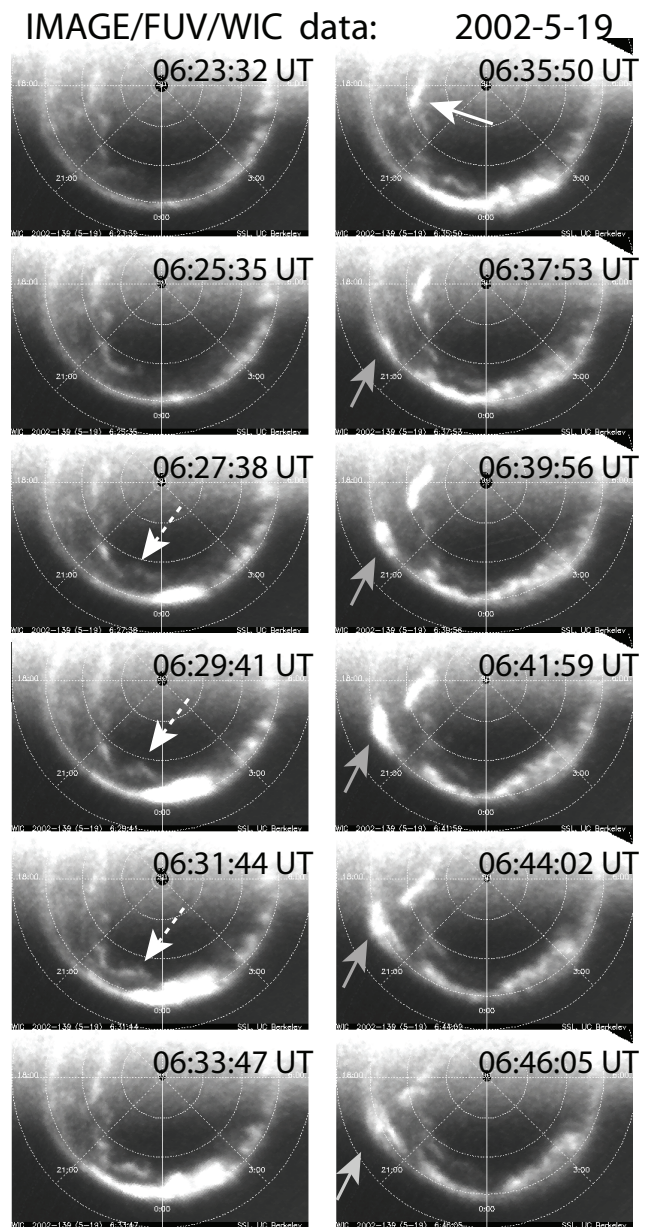


Fig. 4. IMAGE/FUV Wideband Imaging Camera (WIC) data in the magnetic coordinate (GMLat and MLT) during 06:23~06:46 UT on 19 May 2002 taken from the Northern Hemisphere (bottom is 00 MLT and left is 18 MLT, covering 50°~90° GMLat).

is expected to be delayed. ASY-D increased by 50% from 06:28 UT to 06:36 UT, but quickly decayed afterward. Even SYM-H showed short duration (06:28~06:36 UT, not shown here) of increase that is attributed to a decrease of the cross-tail current during the substorm. From these data, this substorm is considered as a minor one.

When the initial substorm activity at midnight started to decay, the second activity started in the evening sector. The poleward arc at 17~19 MLT was activated at around

Table 1. Timeline of the event.

UT	Event
06:25	substorm onset
06:34	peak of midnight activity = start of decay
06:38	start of evening activity
06:42	evening optical bulge arrive at 19 MLT
06:42:50	start of decrease in total B
06:42:50	start of decrease in energetic electron fluxes
06:43:00	start of sharp decrease in total B (SC-3 leading by several s)
06:43:20	start of increase in E-field (SC-3 leading by a few s)
06:43:20	start of increase/decrease in energetic ion fluxes
06:43:20	ion convection exceed detectable speed (SC-3 leading by 10 s)
06:44:00	appearance of 2~10 keV field-aligned ions
06:44:10	peak in E-field at (SC-3 leading by 10 s)
06:44	evening optical bulge started to fold
06:45:55	sudden decrease of the DC E-field
06:46	evening optical bulge started to decay
06:46	sudden appearance of 2~15 keV ions at all pitch angles

06:36 UT as indicated by a white arrow in Fig. 4, and the equatorward arc at 20 MLT was activated at around 06:38 UT as indicated by a grey arrow in Fig. 4. These new brightenings quickly developed during next several minutes. The poleward evening arc became the brightest in the entire night-side during 06:38~06:42 UT, followed by the equatorward evening arc after 06:42 UT, which became a bulge rather than an arc. The new auroral activity is accompanied by new geomagnetic deviations at SIT (~21 MLT) and MCQ (~19 MLT), starting at 06:38 UT and 06:39 UT, respectively. Both stations (about 60° GMLat) are located nearby the new auroral bulge in the equatorward arc.

Thus both the geomagnetic field data and optical data show three discrete activities. One is the substorm onset and subsequent expansion of activity in the midnight at around 06:25 UT~06:34 UT, another is the brightening of evening poleward arc starting at around 06:36 UT, and the other is the formation of the evening auroral bulge and subsequent development starting at around 06:38 UT at around 60° GMLat. Table 1 shows timeline of these epochs as well as the satellite observation described later.

The last two activities developed after the substantial decay of the first activity. Since these three brightening events are not geographically connected to one another, one may not simply assume any causality, i.e., whether the last brightening was leaped from the original substorm bulge or from the brightened poleward oval or combination of both (Yamauchi

et al., 2006) or neither of them. In this paper, we study the last equatorward activity at 60° GMLat because this is conjugate to Cluster.

The evening equatorward activity (auroral bulge) expanded and moved to reach 19 MLT, i.e., the Cluster's local time and latitude at around 06:42 UT. The westward velocity of the bulge front obtained from Fig. 4 is at about 3~4° longitude/min (~3 km/s at ground) for 06:38~06:42 UT, and begin to stagnate (~1° longitude/min) afterward. This corresponds to a sunward motion at 4.4 R_E of about 20~25 km/s for 06:38~06:42 UT, and <10 km/s afterward. The geomagnetic field at MCQ (nearest conjugate) also show a sharp change between 06:42 UT and 06:43 UT, and this timing corresponds to the arrival of the auroral bulge. We do not know the longitudinal extent of geomagnetic disturbance for this auroral bulge because the location of the event corresponds to East Siberia where geomagnetic stations are not well deployed.

3.2 DC electric and magnetic fields

Corresponding to the timing when the auroral bulge arrived the Cluster's conjugate, all Cluster spacecraft observed sudden enhancement of DC electric field and sudden rarefaction of geomagnetic field. Figure 5 shows overview of the field data from SC-4 during 06:42~06:49 UT, and Fig. 6 shows overplot of the total magnetic field and electric field from multi-spacecraft during 06:42:30~06:46:30 UT. The DC field data is sampled at 25 Hz for electric field (EFW) and 22.4 Hz for magnetic field (FGM).

The DC magnetic field which is pointing northward started to decrease gradually from around 06:42:50 UT and sharply from around 06:43:00 UT. The DC electric field started to increase at around 06:43:20 UT, pointing tailward. Within 1 min from the start of increase, DC electric field reached its single peak of up to 10 mV/m at around 06:44:10 UT, then kept relatively high value until the field direction and strength sudden changed at around 06:45:55 UT. Contrary to the electric field, the DC magnetic field has several minima at around 06:43:50 UT, 06:45:00 UT, and 06:46:40 UT, in the semi-periodic way (0.01 Hz frequency range). The decrease reached about 25% (from 180 nT to 135 nT) at around 06:45:00 UT. The density variation somewhat reflects both variations, with minimum at the same time as the main magnetic depletion at around 06:45:00 UT (from 300 cm⁻³ to 200 cm⁻³, or 30%), and a sudden change simultaneously with electric field at around 06:45:55 UT. Thus, these variations are not correlated to each other. No prominent wave activity up to the cyclotron frequency (about 2.5 Hz for H⁺ and 0.15 Hz for O⁺) is observed during this period until 06:45:55 UT.

The inter-spacecraft difference in these DC fields varied in time, indicating that at least two different propagations are convoluted. For example, the peak of the DC electric field at around 06:44:10 UT is clearly led by SC-3 against SC-2 and

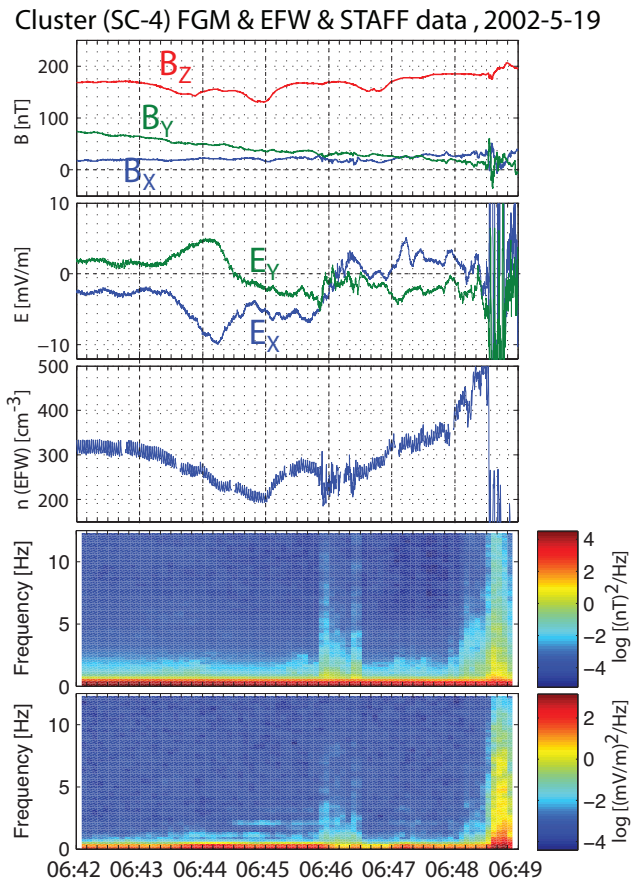


Fig. 5. DC and AC field data during 06:42:00~06:49:00 UT, 19 May 2002, observed by EFW, FGM, and STAFF from spacecraft 4. From top to bottom: DC magnetic field (three components in GSE), DC electric field (spin plane components), estimated plasma density, power spectral density of AC magnetic field, and power spectral density of AC electric field. Since the spin plane is almost perpendicular to the magnetic field, the parallel E cannot be estimated during this period, and the spin plane component is nearly the same as GSE $X - Y$ plane. The sudden drop of the density at around 06:48:30 UT is confirmed by WHISPER.

SC-4 by about 10 s in Fig. 6. This lead is also recognized in the local maximum of the magnetic field at the same time, in which SC-3 leads against other three SC. The lead of SC-3 is seen even at the start of the event: the start of the sharp decrease in the magnetic field at around 06:43:00 is led by SC-3 by several seconds in Fig. 6, and the start of the sharp increase in the electric field at around 06:43:25 is led by SC-3 by several seconds in Fig. 6. However, the local minimum of the magnetic field is found simultaneously at all SC at both 06:43:53 UT and at 06:44:59 UT within half spin. Clearly such Pi2-like multiple peak is caused by different mechanism from the single peaks of the DC electric field.

Therefore, we use the peak time of the DC electric field at around 06:44:10 UT for the timing analyses. Assuming that

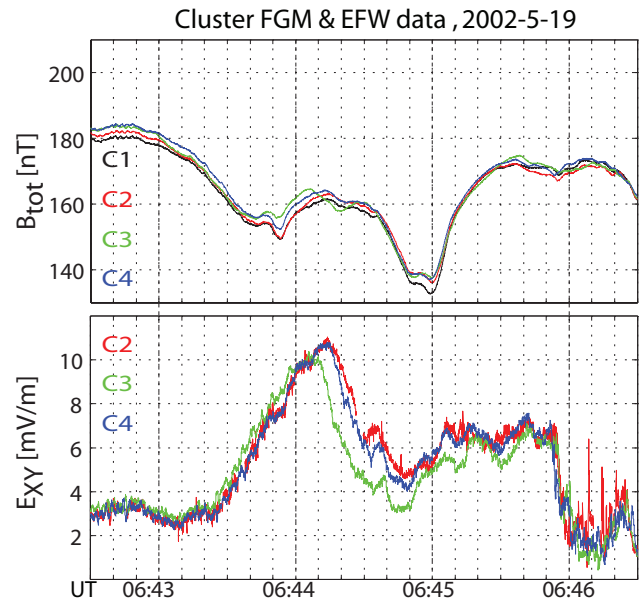


Fig. 6. Multi-spacecraft overplot of DC total magnetic field (upper panel) and total spin-plane electric field (lower panel) during 06:42:30~06:46:30 UT, 19 May 2002 observed by FGM and EFW. Both the magnetic field and the spin axis point nearly northward during this period. Data are de-spined (spin period is about 4 s) after sampled at 25 Hz for the electric field (EFW) and 22.4 Hz for the magnetic field (FGM). SC-1 electric field data is not shown because of de-spin problem. The highest peak of the SC-1 electric field appears at about 06:44:15 UT at nearly the same timing as SC-2 and SC-4 although the SC-1 data is not shown here.

the observed changes in the electric field are due to a spatial structure moving past the spacecraft, and that the structure is flat on the length-scale of the separation of the satellites, we can use the spacecraft constellation (Fig. 2) and timing to estimate the velocity of the structure. Fortunately, the timing between SC is the same between the DC electric field and the DC magnetic field for the peak at about 06:44:10 UT, and we can use the timing in the magnetic field to obtain the propagation velocity. Our estimation falls about 5~10 km/s (about 50~100 km distance in about 10 s) in mainly sunward (+X) with large dawnward (-Y) tilt.

On the other hand, the nearly simultaneous timing between spacecraft at the magnetic minima at around 06:43:53 UT and 06:44:59 UT might mean quick propagation along the magnetic field. From the density (200~300 cm⁻³) and magnetic field (140~180 nT), Alfvén velocity is estimated 200~250 km/s. Since the spacecraft separation in the Z direction is only 50~250 km, the propagation time is only about 1 s between northernmost SC-1 and southernmost SC-3 if propagation is along the magnetic field with Alfvén velocity. This means that the Alfvén signature (this carries the DC field) is observed nearly simultaneously between SC. In this case, one must also consider the possibility

that quick bouncing of Alfvén wave along the magnetic field constituted the sunward progression as is employed in some magnetosphere-ionosphere coupling models (e.g., Sato, 1978). However, this scenario does not explain the behavior of the energetic particles that is shown later in Sect. 3.5. The behavior of the observed DC field is also different from the prediction by the magnetosphere-ionosphere coupling models (e.g., Sato and Iijima, 1979). The reflected Alfvén wave has nearly opposite phase relation (skewed by Hall conductivity effect) between the deviated DC electric and magnetic fields, causing a sawteeth-like field variations superimposed on the original field change (Sato and Iijima, 1979), but the observed change from 06:42:50 UT to 06:43:50 UT is nearly monotonic.

The DC electric field pointed mainly tailward until 06:45:55 UT, gradually rotating from duskward deflection (positive E_Y) to purely tailward (small E_Y), ending with dawnward deflection. The observed electric field is parallel to the propagation direction of the peak electric field. Therefore, the propagation is longitudinal, i.e., electric charge is accumulated at the front of the propagation. Such a charge accumulation normally causes a strong downward field-aligned current, but such current is not visible in the magnetic field data (in B_X and B_Y). The accumulated charge most likely further propagate sunward before it is lost in the form of the field-aligned current.

The 10 mV/m electric field in the equatorial plane is a level of substorm onset and is quite high considering its location at 19 MLT (Pedersen et al., 1984; Maynard et al., 1996). If we map this electric field to the ionosphere, it would be nearly 100 mV/m (corresponding to about 2 km/s convection), reaching to the same level of small-scale (<30 km) DC electric field in the ionosphere with aurora during substorms, but it is unrealistically large as a large-scale electric field (Kamide et al., 1996; Sanchez et al. 1996; Marklund, 1997). Thus, there must be parallel potential drop between the ionosphere and the spacecraft location, in agreement with the brightening of the aurora at the satellite conjugate.

A 5 ~ 10 km/s sunward velocity is comparable to magnetic drift of 15 ~ 30 keV ions or electrons (mass independent) in both the direction and the speed. The one-minute time scale from the start of the event to its peak with this velocity mean that the gradient of the electric field has a scale size of about 500 km or less. If this propagation speed is similar during the entire electric field structure during 06:43~06:46 UT, the total electric potential drop in the X direction during the passage of this structure is about 5~10 kV ($5\sim 10\text{ km/s}\times 200\text{ s}=1000\sim 2000\text{ km}$ with average field of 5 mV/m), positive front and negative back.

The irregular magnetic oscillation of about 0.01 Hz frequency range is typical during substorms and is called Pi2 pulsation (Olson, 1999). The observed Pi2-like pulsation is detected mainly in total intensity (which points northward) in a rarefied sense but not in the X - or Y -component. Thus the entire geomagnetic field simply oscillates between outward

(rarefying) and inward (recovering). Such a simple oscillation means a perpendicular current without field-aligned current. This Pi2-like variation is not visible at MCQ in Fig. 3 due to low temporal resolution of the data (1 min resolution).

The combination of the strong DC electric field and Pi2 range magnetic oscillation is a typical phenomenon at the substorm onset (e.g., Olson, 1999, Roux et al., 1991). However, neither the electric field nor magnetic pulsation started at the onset of the substorm (at around 06:25 UT) or when the bulge is formed (at around 06:38 UT). The activity did not start until the arrival of the auroral bulge at the conjugate ionosphere. This indicates that they are related to local auroral bulge but not global substorm onset (Shiokawa et al., 2002).

At around 06:45:55 UT, the spin-plane electric field suddenly dropped from 7 mV/m to 3 mV/m within several seconds in Fig. 6. Accompanying this change, a low-frequency electromagnetic wave burst is observed and the density drops, but the DC magnetic signature is barely seen in Fig. 5. The change is very sharp compared to the peak at around 06:44:10 UT (gradient lasts about 40 s), and is simultaneous at all spacecraft by a few second in Fig. 6. The quick change of the electric field indicates a boundary crossing. The crossing direction is probably outward according to the timing of the small magnetic dip at around 06:45:55 UT (SC-4 is leading, followed by SC-2), although the difference is within one spin. The slightly different behavior at SC-3 might be due to spatial structure rather than the temporal structure. On the other hand, the change in the electric field direction (or strength of E_X) is relatively smooth (taking about 40 s) across this boundary.

3.3 Helium-rich cold ion convection

The strong DC electric field of 10 mV/m perpendicular to the background magnetic field (mainly northward) of 160 nT at around 06:44:10 UT means an $\mathbf{E} \times \mathbf{B}$ drift velocity of about 60 km/s for all ion species. With such a high velocity, thermal ions have enough energy to be detected by CIS with ordinary observation mode, which has the lowest energy threshold of about 4 eV/q for HIA and about 25 eV/q for CODIF. An $\mathbf{E} \times \mathbf{B}$ velocity of 50 km/s means that we should be able detect H^+ at ~13 eV (i.e., only by HIA), He^{++} at ~25 eV (i.e., only by HIA), He^+ at ~50 eV (i.e., by both HIA and CODIF), O^{++} at ~100 eV (i.e., by both HIA and CODIF), and O^+ at ~200 eV (i.e., by both HIA and CODIF) if they exists as the thermal plasma.

Therefore, CIS must detect concentrated ion counts at these expected energy (10~200 eV) and direction if the thermal plasma exists. Since the magnetic field points nearly northward with electric field points nearly anti-sunward ($E_X < 0$) with some change of E_Y sign from + Y direction to - Y direction according to Fig. 5, the expected convection direction is mainly duskward with some rotation from dusk-sun direction (06:43:30~06:44:30 UT) to dusk-tail direction

(06:45:00~06:46:00 UT). This is the expected direction of the flow.

In Fig. 1b, enhanced ion counts in the tens eV range are observed in the perpendicular direction to the magnetic field during 06:43:20~06:46:10 UT. Since the energy range and pitch angle agrees with the expected $\mathbf{E} \times \mathbf{B}$ flow, this is the best candidate for the expected convection. To see the observed azimuthal direction, the full-resolution ion data (not averaged over spin or sectors) is shown in Fig. 7 from SC-1 (HIA data), SC-3 (HIA data), and SC-4 (CODIF data), for the sectors that have substantial counts beyond the noise level. Measurement from each direction is performed every 12 s for HIA data and every 8 s for SC-4 CODIF data.

In Fig. 7, counts at low-energy (<100 eV) range in the perpendicular direction to the magnetic field (Fig. 1b) are registered consistently from the same azimuthal direction (corresponding to limited spin phase angle). Thus, the observation indicates a convection flow in the direction illustrated in Fig. 7 (below the 4th row). Furthermore, the observed counts are detected in very limited range in energy and direction in each 4-s observation, indicating that they are cold ions.

The observed flow direction shown in Fig. 7 gradually rotates. Starting as a sun-duskward (15 LT direction) flow at around 06:43:30 UT, it became duskward (rotate by 45°) at around 06:44:30 UT, and tail-duskward (20 LT direction) at around 06:45:30 UT (not shown here). After this, the detected area in direction widened toward tailward direction, and finally all counts faded at around 06:46:10 UT. The history of the flow direction agrees with that of the $\mathbf{E} \times \mathbf{B}$ direction.

During the short period of 06:43:44~06:44:20 UT for SC-1, 06:43:43~06:44:07 UT for SC-3, and 06:43:47~06:44:27 UT for SC-4, the energy of these convecting ions increased, and second ion counts appeared at energy about one quarter of the energy of first counts (e.g., at 06:44:08 UT, peaks are at around 70 eV and 17 eV). The timing corresponds to the largest enhancement of the electric field (and hence $\mathbf{E} \times \mathbf{B}$ drift) at around 06:44:10 UT. The ratio of 4 means either O⁺/He⁺ pair or He⁺/H⁺ pair because the $\mathbf{E} \times \mathbf{B}$ cause the same velocity for all ion species. From the energy matching described before, these ions must be He⁺ (higher energy, 06:43:20~06:46:10 UT) and H⁺ (lower energy, 06:43:40~06:44:20 UT), giving us a value of velocity about 57 km/s at 06:44:08 UT. The CODIF composition data in Fig. 7 (SC-4) confirms this composition. Furthermore, CODIF detected only He⁺ and H⁺ but not O⁺, O⁺⁺ or He⁺⁺ for all SC-1, SC-3, and SC-4 (not shown here). Thus, the data shows abundance of plasmaspheric cold He⁺ inside the ring current region at $R > 4 R_E$, while no cold O⁺ was detected by the same instrument during this period.

In the spacecraft frame, one should also include the satellite velocity when considering low-energy. During this period, Cluster moved northward (i.e., nearly the field-aligned direction) with 5 km/s, which is very small compared to the

convection velocity. The expected shift of the relative direction against the magnetic field in the spacecraft frame is 5° (for 50 km/s convection or 10 mV/m electric field) to 15° (for 20 km/s convection or 4 mV/m electric field). This minor shift is actually recognized in the 4th row of Fig. 7 (peak is seen at about 95° ~ 100° pitch angle instead of 90°).

Figure 7 also shows a slight time shift between SC-1 and SC-3. At 06:43:19 UT, the ion flow appeared at SC-3. One second later (06:43.20 UT), the signal of the ion flow at SC-1 was too weak to appear in the figure although the HIA instrument was looking the right direction. The timing for the weakening is also led by SC-3. The double peaks (H⁺ counts in addition to He⁺ counts) are seen in SC-1 until 06:44:20 UT, while they already disappeared one second before (06:44:19 UT) in SC-3, indicating about one cycle (12 s) difference.

We can also examine the timings for SC-4 although the instrument is different: the expected flow is not detected until 06:43:31 UT partly due to lower sensitivity than HIA at SC-1 and SC-3, but double peak (H⁺ in addition to He⁺) is detected until 06:44:27 UT. The highest counts are detected at 06:44:03 and 06:44:11 UT. This timings are close to the SC-1 timing and delayed from SC-3 timing by about 10 s. The timings of SC-3 (10 s lead), SC-1 and SC-4 are consistent with those in the local peaks of the DC electric and magnetic fields at around 06:44:10 UT in Fig. 6, confirming our timing analyses in Sect. 3.2.

3.4 Ionospheric keV ions

If the auroral bulge in the conjugate ionosphere (Fig. 4) is associated with the large change in the DC field (Figs. 5 and 6), a field-aligned potential drop should exist between Cluster and the ionosphere to accelerate auroral electron to the ionosphere to several keV. This field-aligned potential drop simultaneously accelerates ionospheric ions upward to several keV (about 1000 km/s for 5 keV H⁺ and 250 km/s for 5 keV O⁺). Since these ions travels 4 R_E distance in about 30 s for H⁺ and about 2 min for O⁺, Cluster should detect these ionospheric ions in the field-aligned direction close to the event. Indeed Fig. 1c shows enhancement of nearly field-aligned component at 2~20 keV at around 06:44 UT.

We should note that an enhancement of the nearly field-aligned component does not necessarily mean arrival of ionospheric ions because the depletion of the magnetic field also causes shift of ion's pitch angle toward low pitch angle due to the conservation of the first adiabatic invariant (or the magnetic moment) $\mu = W_{\perp}/B$, where W is the energy of the charged particle and \perp denotes the perpendicular component to the magnetic field. Since the gyro period under 160 nT magnetic field is about 0.4 s for H⁺ and 6 s for O⁺, the change of the magnetic field (1 min) is small enough for the magnetic moment to be conserved. On the other hand, the second invariant is not conserved for these ions because bouncing period is in the order of minutes. In this case, the

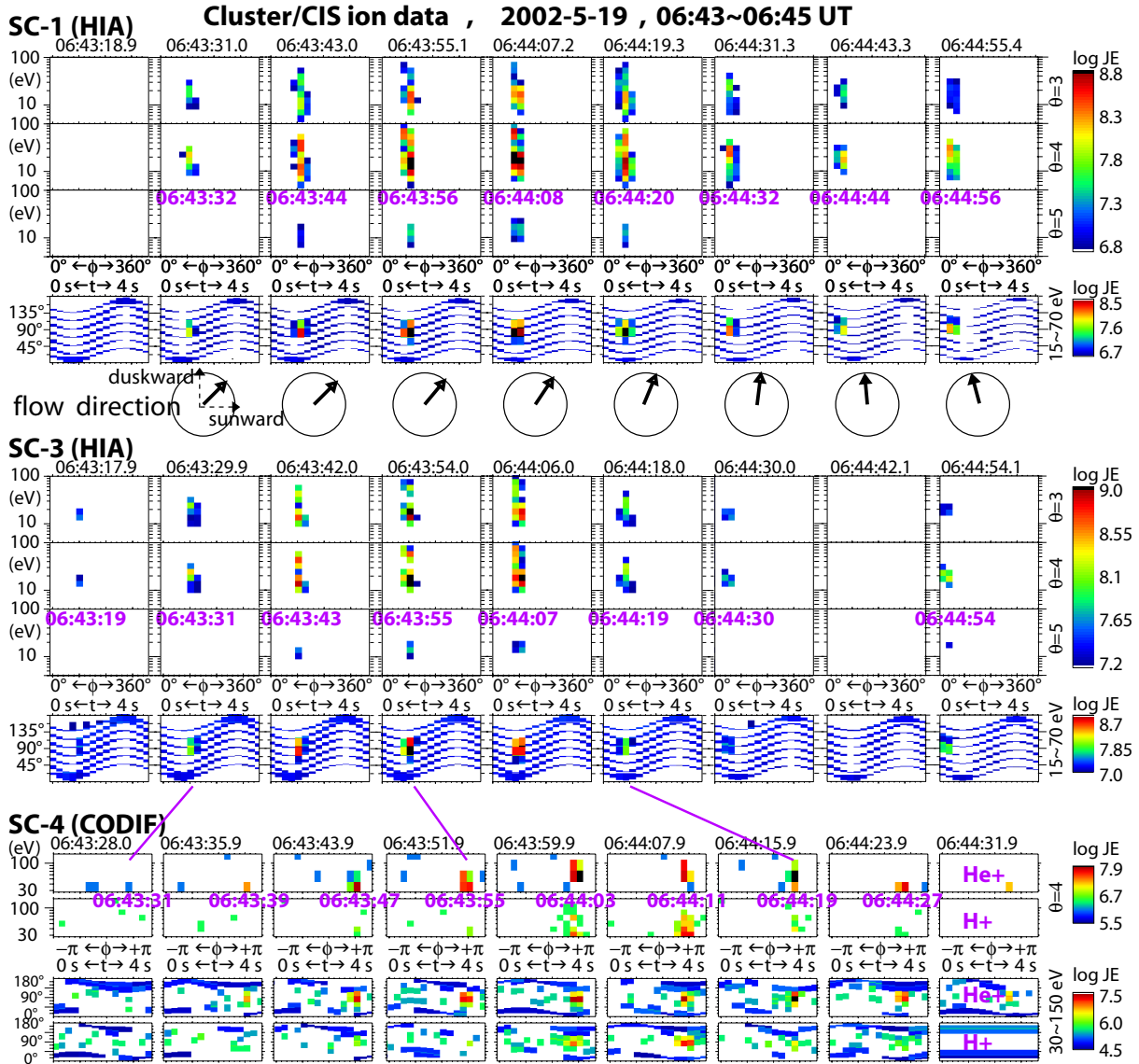


Fig. 7. Highest resolution plots of differential energy fluxes ($\text{keV cm}^{-2} \text{s}^{-1} \text{str}^{-1} \text{keV}^{-1}$) of low-energy ions observed by CIS during 06:32:18~06:44:59 UT (total 100 s) on 19 May 2002 for SC-1 HIA data (upper 4 rows), SC-3 HIA data (middle 4 rows), and SC-4 CODIF data (bottom 4 rows) corresponding to low-energy part of Fig. 1b. Data is not averaged over spin (4 s) or different sectors (polar angles). During this period, HIA took data every third full-spin (taking data 4 s and idle 8 s) for both SC-1 and SC-3, while CODIF took data less frequently except for SC-4 which took data every other full-spin (taking data 4 s and idle 4 s). For each 4-s measurement, UT corresponds to the spin phase angle (azimuthal angle, which is 180° off between HIA and CODIF), and the starting UT of each 4-s measurement is displayed at the top of panels for each SC. The top three rows are energy-time spectrograms of 4~100 eV ions from SC-1 observed at sectors with non-zero flux beyond the noise level (sectors 3, 4, and 5) among total 8 sectors. Sector 1 is looking at nearly north, i.e., detecting ions traveling nearly along the geomagnetic field from north to south. Sectors 4 and 5 correspond to nearly perpendicular direction to the geomagnetic field. The UT under the enhanced counts inside panels corresponds to the UT when these counts are actually detected (in only 2~3 directions out of 16 azimuthal directions). The 4th row is energy-averaged (15~70 eV) pitch angle-time (azimuth) spectrogram, where the blue thick lines denote the direction of boundaries between neighboring sectors (top and bottom sectors corresponds to sectors 1 and 8, respectively). The pitch angle of each sector slightly modulated because the spin axis is not exactly 90° from the magnetic field direction. The enhanced counts are registered in nearly the same azimuthal direction, and this flowing direction in the geophysical coordinate is illustrated below the 4th row. The middle four rows are the same as the first four rows except they are from SC-3. The last four rows (CODIF data from SC-4) are organized as energy-time spectrograms of 30~150 eV H^+ and He^+ from sector 4 (the sector with most intense counts), and energy-averaged (30~150 eV) pitch angle-time (azimuth) spectrograms for H^+ and He^+ , respectively.

parallel energy W_{\parallel} does not change by the magnetic field variation. Under this condition, a 25% decrease in the magnetic field means a 25% decrease of W_{\perp} (e.g., from 5 keV to 4 keV) while keeping W_{\parallel} . The pitch angle (θ) also changes as $2 \times d\theta \times (\tan\theta + \cotan\theta) = (dB/B)$, or maximum about 7° .

These changes are so small that we could not explain the most of the sudden change of flux at around 06:44 UT except the change of the pitch angle at 10~20 keV at around 06:44~06:45 UT in Fig. 1c toward field-aligned direction. For example, the sudden enhancement of low pitch angle 2~4 keV ions at around 06:44~06:45 UT cannot be explained by this effect. Therefore, the increase in the low pitch angle ions is due to a net arrival of ions. Similarly, sudden drop of the ion flux at 20~40 keV at around 06:44 UT in Fig. 1c is also net change that cannot be explained by the conservation of magnetic moment. On the other hand, it is difficult to judge the cause of the enhancement of low pitch angle 4~8 keV ions at around 06:44~06:45 UT.

To examine the most parallel component (both parallel and anti-parallel) to the magnetic field at this energy range more, Fig. 8 shows differential fluxes of H^{+} and O^{+} from selected sectors observed by CIS/CODIF from SC-4. Five directions are shown: sector 1 (most anti-parallel direction to the magnetic field looking north), sector 2, sectors 4 and 5 (perpendicular direction), sector 7, and sector 8 (most parallel direction to the magnetic field looking south). As is already expected from Fig. 1c, the parallel flux and anti-parallel flux are very similar in Fig. 8.

Before 06:43:40 UT, ions are trapped as seen in Fig. 1c although the fluxes of the most parallel directions (directions 1 and 8) are higher than those of the other directions at around 10 keV for both H^{+} and O^{+} . They are ions bouncing between mirror points. At around 06:43:40 UT, the fluxes of most parallel components (both parallel and anti-parallel) started to be enhanced at a wide energy range for H^{+} (2~15 keV) and at low-energy for O^{+} (2~8 keV) as indicated by arrows, whereas fluxes of the perpendicular component suddenly decreased.

The conservation of the magnetic moment moves the direction of intense flux from directions 2 to 1 and from directions 7 to 8 when the magnetic field decreased from 06:43 UT to 06:45 UT, and vice versa when the magnetic field increased after 06:45 UT (see Fig. 6). We do not recognize such effect for the sudden flux enhancements marked by arrows at around 06:44 UT. Certainly, these enhancements are net increases of flux, indicating a new injection along the magnetic field. The energy range is typical of auroral acceleration potential. Together with composition (substantial O^{+}) and direction, the observed field-aligned ion burst at around 06:44 UT is most likely caused by the parallel potential above the auroral bulge seen in the IMAGE/FUV data in Fig. 4. The upward direction agrees with general particle signatures and field-aligned current direction at the front side of the westward traveling surges (Kamide and Rostoker, 1977; Meng et

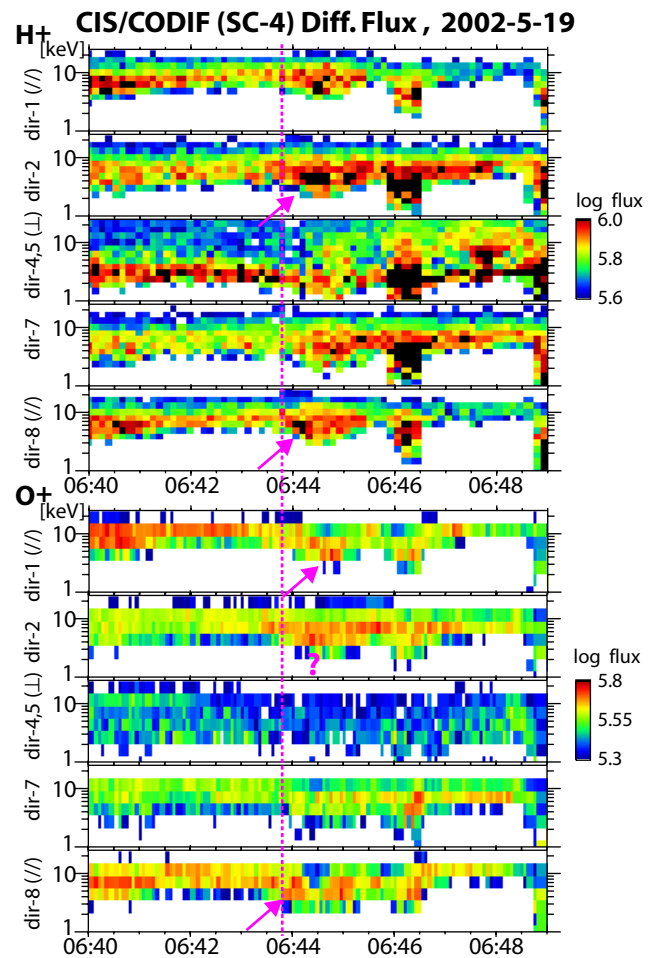


Fig. 8. Energy-time spectrogram of differential particle flux ($\text{cm}^{-2} \text{s}^{-1} \text{str}^{-1} \text{keV}^{-1}$) of 1~25 keV H^{+} (upper 5 panels) and O^{+} (lower 5 panels) observed by CIS/CODIF from SC-4 during 06:40~06:49 UT on 19 May 2002. For both H^{+} and O^{+} , five directions are shown: nearly anti-field-aligned from north to south (sector 1), oblique (sector 2), nearly perpendicular to the magnetic field (sectors 4 and 5), oblique (sector 7), and nearly field-aligned from south to north (sector 8), respectively. The O^{+} count is not contamination from H^{+} except 3 keV peak at around 06:44:10~06:44:40 UT at direction 2 (question mark) according to time-of-flight spectrum (not shown here). The sudden intensifications marked by arrows are real for both H^{+} and O^{+} .

al., 1978; Inhester et al., 1981; Opgenoorth et al., 1989; Fujii et al., 1994).

Since 5 keV ions takes about 20~30 s for H^{+} and about 100 s for O^{+} to travel from ionosphere to the Cluster location at $L=4.4$, we expect time delay between H^{+} enhancement and O^{+} enhancement if the spacecraft observed temporal change. However, the arrival time of the ionospheric ions are nearly simultaneous between O^{+} and H^{+} , i.e., difference is much less than the expected time-of-flight difference. The arrival time is even the same between parallel direction (from

southern ionosphere) and anti-parallel direction (from northern ionosphere) to the magnetic field. Simultaneous appearance of O^+ and H^+ means that spacecraft crossed a boundary that is filled with field-aligned ions. However, constructing such configuration is not simple because this boundary is propagating sunward (Sect. 3.2). In 100 s, the boundary moves 500~1000 km sunward, which is larger than the gyroradius of the 5 keV O^+ (about 250 km).

Therefore, we have to consider the convection and backtrace the field-aligned H^+ and O^+ that simultaneously arrived the Cluster. Here one may not ignore the effect of strong $E \times B$: the 3~8 keV ions in Fig. 8 came from lower L than Cluster by about $0.3^\circ \sim 0.5^\circ$ in latitude if we consider $E \times B$ drift during the travel of ions. Since the convection direction is nearly perpendicular to the propagation direction (Sect. 3.3), just a small folding of the boundary can give the nearly simultaneous arrival time between H^+ and O^+ . Folding of aurora is quite common and in fact the front of the auroral bulge in Fig. 4 is not straight but round. Furthermore, the exact arrival time is slightly different (be 10~20 s) between field-aligned H^+ and field-aligned O^+ . This supports the above scenario. At around 06:45:30 UT, the parallel H^+ disappeared without trailing low energy H^+ . That again means the boundary crossing, i.e., exit from the downstream of field lines with the parallel potential in this case.

At around 06:46 UT, one can also recognize another sudden increase in <5 keV H^+ fluxes. The increase is seen at all (both parallel and perpendicular) directions. This timing corresponds to the boundary crossing at around 06:45:55 UT that is indicated by the sharp changes in the DC electric field, wave, and density as are seen in Figs. 5 and 6 (Sect. 3.2). The flux increase in the perpendicular component is recognized over broad energies up to 40 keV (upper limit of detection), whereas the flux increase in the parallel component is limited to <10 keV. Parallel component of O^+ flux increased slightly (10~20 s) after this dispersionless H^+ flux increase.

3.5 Mass-dependent change in Ring Current flux

The sudden change at around 06:43 UT is also recognized in the fluxes of energetic particles as shown in Fig. 1a. Starting at around 06:43 UT, the flux of medium energy ions (H^+ at 75~92 keV, He^+ at 170~240 keV, and O^+ at 640~950 keV) observed by RAPID increased, while the flux of high-energy ions ($H^+ > 160$ keV and $He^+ > 350$ keV) and energetic electrons (>40 keV) observed by RAPID decreased. Flux of low energy ring current ions (20~40 keV) also decreased as shown in Fig. 1c (the decrease is mainly in O^+ according to the CODIF data). These observations immediately show that (1) the fluxes changed rapidly within a few minutes; (2) the change direction (decrease or increase) of the flux depends on energy; and that (3) the threshold energy between increasing flux and decreasing flux (or characteristic energy of flux increase) is mass dependent, with higher threshold energy for higher mass.

The mass dependency of the sudden flux increase or decrease of the ring current ions (about 100 keV) has never been reported or expected because magnetic (gradient-B and curvature) drift velocity is proportional to energy without mass dependency. To examine this, we show high-resolution RAPID data in Figs. 9 and 10 (H^+ channel in Fig. 9a, He channel in Fig. 9b, CNO channel in Fig. 9c, and electron channel in Fig. 10a) from all relevant energy channels during 06:41:00~06:49:00 UT. According to Fig. 9, the threshold energy between the flux increase and decrease is about 100 keV for H, about 400 keV for He, and probably about 1.5 MeV for O; i.e., it is nearly proportional to the mass (proportional to $M^{0.7 \sim 1}$). The same mass dependency (or mass proportionality) is seen in the energy of the largest increase, i.e., the characteristic energy. It is about 50~80 keV for H^+ , about 150~200 keV for He^+ , and about 500~800 keV for O^+ .

The mass proportionality means that the increase/decrease difference is determined by the speed of ions, but not the energy (or drift velocity) of the ion. The threshold speed is about 4500 km/s, and the characteristic speed is about 3000 km/s. For electrons, fluxes of all energy channel of RAPID decreased, as shown in Fig. 10a. This is reasonable if the same mass dependency is applicable to the threshold energy of electron, which falls to about 0.04 keV characteristic energy for the increasing flux.

On the other hand, the energy-dependent flux change of the ring current population during storm-time substorms has been known for three decades (Lyons and Williams, 1976; Lyons, 1977). Such dual behavior has been explained by the conservation of first and second adiabatic invariants during the magnetic variation (Ebihara et al., 2008). As described in Sect. 3.4, the conservation of the magnetic moment (first adiabatic invariant) causes increase of W_\perp when the magnetic field is compressed. This conversion means that the distribution function $f(W_\perp)$ shift toward lower W_\perp than the original position. Thus, decrease of B means an increase or a decrease of $f(W_\perp)$ at the fixed energy when $df/dW_\perp > 0$ or $df/dW_\perp < 0$, respectively. For the ring current particles which are trapped (it is so for the present case), we can use $f(W)$ instead of $f(W_\perp)$ to examine df/dW_\perp .

Since ions with 3000 km/s velocity bounce within the geomagnetic bottle in about 10~15 s in one hemisphere, it is possible that second adiabatic invariant is also conserved. In this case, magnetic field variation changes parallel energy W_\parallel through the change of mirror altitude: a lift of mirror altitude causes shortening of the mirror bouncing distance, and hence increase of parallel momentum through the Fermi process (Alfvén and Fälthammar, 1963). Since the lift of the mirror altitude is caused by compression of the magnetic field, the observed decrease of the magnetic field means both $dW_\perp < 0$ and $dW_\parallel < 0$. Therefore, the consideration of the second adiabatic invariant does not change the present examination on $f(W)$.

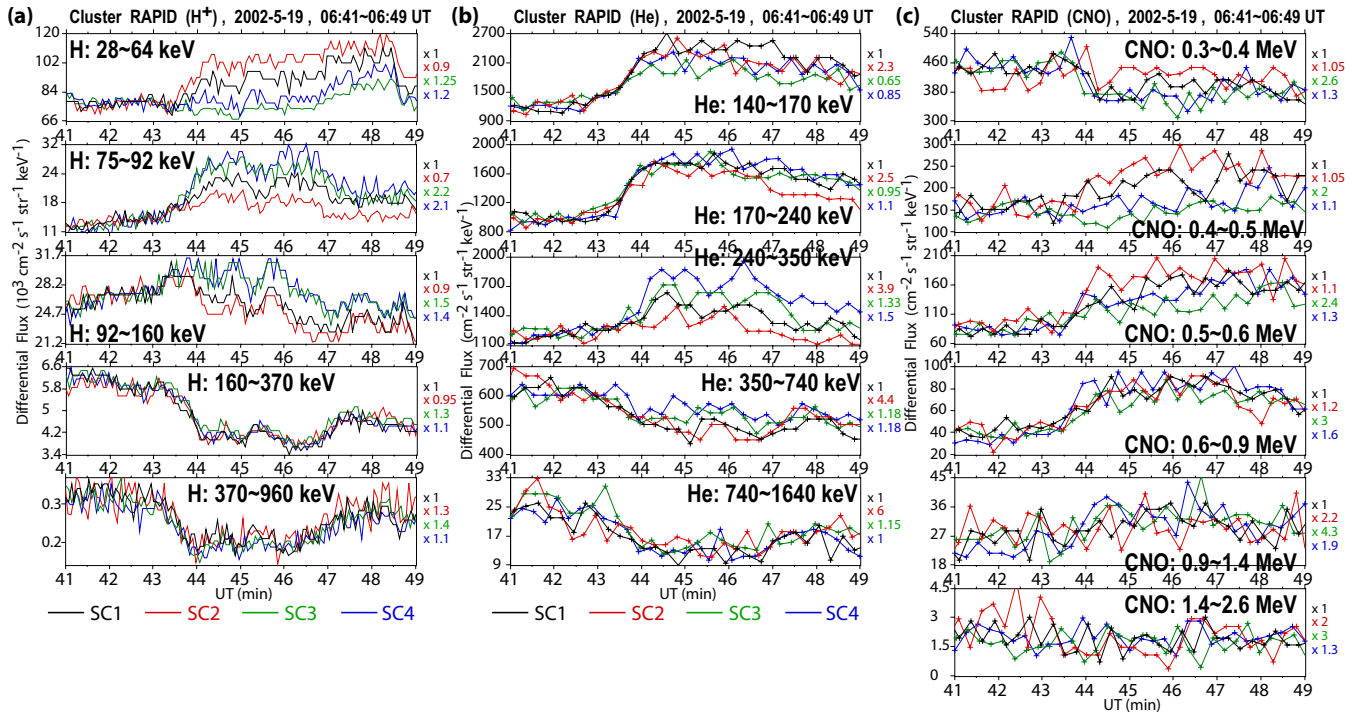


Fig. 9. Overplots of 4π -averaged differential ion fluxes observed by RAPID from four spacecraft during 8-min period (06:41:00~06:49:00 UT). Only the relevant energies are listed. The data (black lines for SC-1, red lines for SC-2, green lines for SC-3, and blue lines for SC-4) are adjusted using scaling factors given in the right side of each panel. These factors are determined from the data before 06:43 UT when all SC are assumed to detect the same flux value. The factors are not unity although we used the calibrated data. The CNO channel covers mass range of C, N, O, but we can generally ignore contributions from C and N in the magnetosphere.

Let us examine this scenario. Figure 11 shows the distribution function observed by RAPID during 06:42~06:43 UT, i.e., just before the event started. We also showed flux because distribution function has a larger error bar than flux due to wide range of energy for each energy channel (distribution function is obtained by dividing flux by energy). In Fig. 11, almost all energy at all species (except for >330 keV electrons and 92~160 keV protons) have $df/dW < 0$, with possible $df/dW > 0$ within error bar for 240~350 keV He. This predicts decrease of flux during magnetic depletion except for >330 keV electrons and 92~160 keV protons. Therefore, the flux increase of 3000 km/s ions during 06:43:00~06:45:00 UT cannot be explained by the conservation of the magnetic moment. The inconsistent flux change with the magnetic moment conservation is also seen in the 1~2 min modulation as will be shown in Sect. 3.6..

The finite gyroradius effect of 3000 km/s ions (200~250 km for protons and 900 km for He⁺) breaks down the conservation of magnetic moment but this effect does not explain the flux increase. Furthermore, the wave activity (Fig. 5) is too small to explain the flux increase by local acceleration, e.g., there is no wave at cyclotron frequency (about 2.5 Hz for H⁺ and 0.15 Hz for O⁺ under 160 nT magnetic field). Temporal change of DC field during

one gyration is less than 1%, too small to accelerate ions. Therefore, the observed flux increase of 3000 km/s ions during 06:43~06:45 UT is most likely due to a new injection from outside.

We also observed energy-time dispersion in the initial flux increase from high energy to low energy. The 28~64 keV (10~20 km/s drift speed) H⁺ flux started to increase at around 06:43:30 UT, 75~92 keV H⁺ (20~30 km/s drift speed) at around 06:43:20 UT, 92~160 keV H⁺ (30~50 km/s drift speed) at around 06:43:10 UT, and even the 160~370 keV H⁺ (50~100 km/s drift speed) flux shows very minor increase at around 06:43:00 UT. Similar dispersion can be recognized in He flux sharp increase between 140~170 keV (around 06:43:40 UT) and 170~240 keV (around 06:43:30 UT), but this relation does not hold for 240~350 keV He flux.

The observed energy-time dispersion of the initial flux increase is not due to time-of-flight but by the finite gyroradius. The time-of-flight distance from the drift velocity is less than 1000 km for the H⁺ energy-time dispersion. This distance corresponds to only a few minutes propagation for the structure, and neither the particle nor the field data showed any signature of local acceleration within 1000 km distance from the epoch of flux increase. Furthermore, this

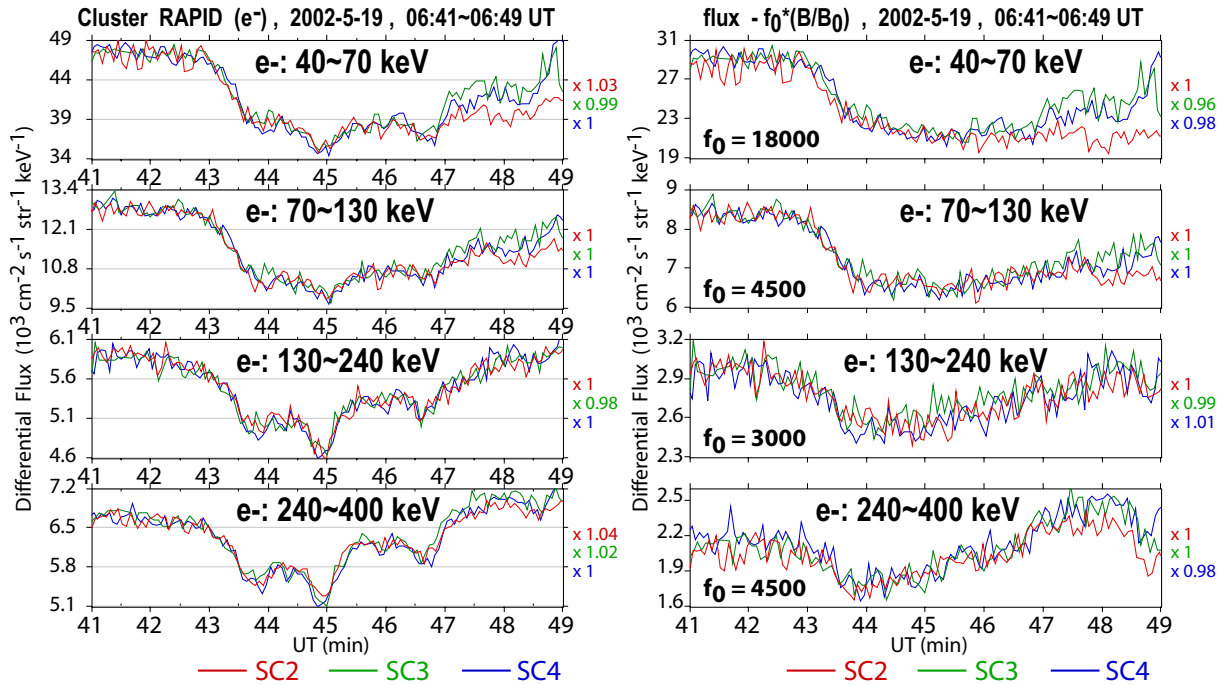


Fig. 10. (a) The same as Fig. 9 but for electron data. (b) Linearly separated profiles of the observed electron flux from the variation that is proportional to the magnetic field variation assuming $\text{flux} = f_0 + f_1 \times (dB/B_0)$, where $dB = B - B_0$, and $B_0 = 190$ nT is the magnetic field at the start of the event (06:42:50 UT).

distance is comparable to the gyroradius of these ions (Table 2) and to the scale size of the gradient of DC field and flux (~ 500 km). Therefore, the time-of-flight effect is not the explanation. Instead, we consider the finite gyroradius effect which also makes this type of dispersion: high-energy ions reach farther than low energy ions. In the present case, every 70~80 km decrease of proton gyroradius caused 10 s delay, which agrees with the propagation velocity of about 5~10 km/s. The large delay between H^+ and He^+ in this case should be attributed to different reasons.

It is worth estimating the increase of the plasma pressure due to the increased flux and to compare it with the decrease in the magnetic pressure during first two minutes (06:43:00~06:45:00 UT) until the magnetic minimum. The H^+ flux increased by $(2\sim 4) \times 10^4 \text{ cm}^{-2} \text{ s}^{-1} \text{ str}^{-1} \text{ keV}^{-1}$ at 30~90 keV range during first minute of the event. This corresponds to increase of partial pressure of about by 1.5~2 nPa. The O^+ flux increased by $50\sim 150 \text{ cm}^{-2} \text{ s}^{-1} \text{ str}^{-1} \text{ keV}^{-1}$ at 400~900 keV range during the same period (corresponding to about 0.02 nPa). The total magnetic field changed from about 180 nT before the event to about 155 nT at the first dip and about 140 nT at the second and the largest dip. The change in the magnetic pressure is about -3.5 nPa until the first dip and about -5 nPa until the second dip. Considering the large uncertainty of the instrumental sensitivity on solid-state detector (SSD), difference in factor two is a quite good

match between the plasma pressure increase of relevant ions and the magnetic pressure decrease.

3.6 Synchronized modulation of flux by magnetic field

All panels in Fig. 10a show a modulation of the electron fluxes with about 1~2 min period (about 10^{-2} Hz) beyond the noise level instead of monotonic decrease. This modulation is very similar to the Pi2-like magnetic field variation in Fig. 6. Each dip of electron flux (06:43:50 UT, 06:44:55 UT, 06:45:55 UT, 06:46:40 UT) took place at the same time (within the 4-s spin resolution) as the corresponding dip of total magnetic field strength (which is pointing nearly northward in GSE). Thus, the observed electron flux modulation is well synchronized with the magnetic field variation. The good match is seen only with the magnetic field but not with electric field in Fig. 5.

The variation of the electron flux synchronized with Pi2-like magnetic field variation is more prominent at higher energy than lower energy. To make this clear, we separate the flux variation into two components, one that is locked with the magnetic field variation and the other that gives general change independent of the magnetic field variation. Since the variation of the magnetic field is only 25% from the start of the event (06:42:50 UT) to its minimum (06:44:50 UT), we here assumed linear combination: $\text{flux} = f_0 + f_1 \times (dB/B_0)$.

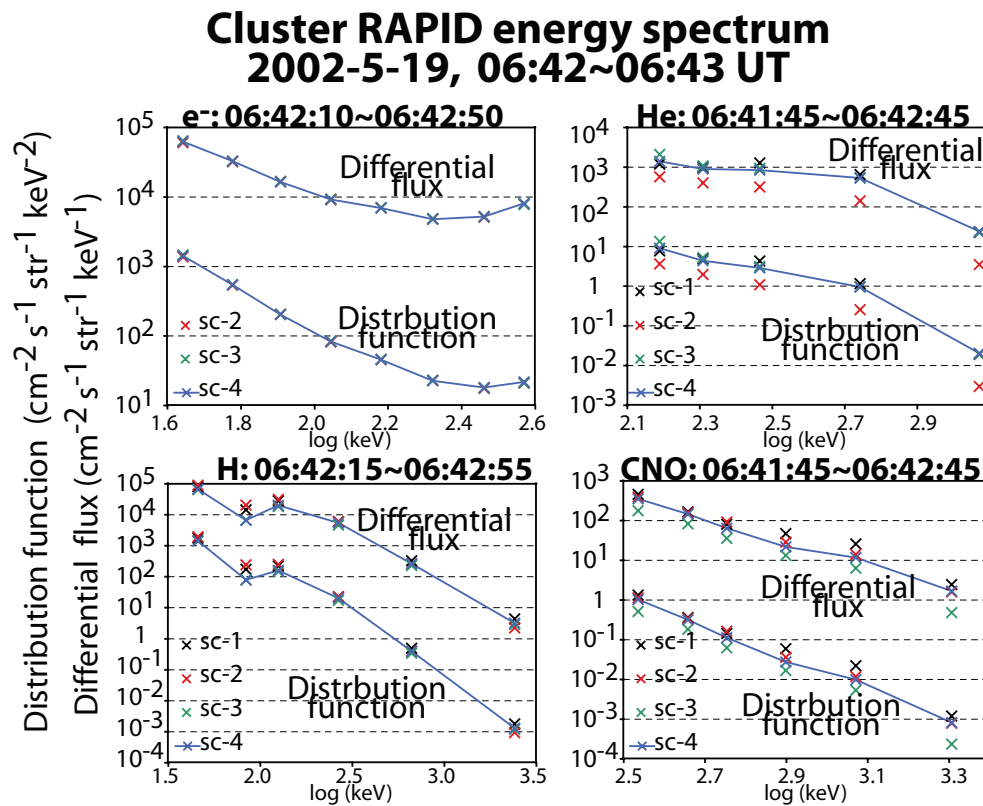


Fig. 11. Normalized distribution function for (a) electron, (b) proton, (c) helium, and (d) oxygen during 06:42:18~06:42:52 UT (averaged over 9 spins) just before the 06:43 UT event. Here we simply divided the differential flux by energy, which is proportional to the distribution function by a factor of $0.5M^2$, where M is the mass of the ion. Since error bar is large in the energy direction, which is the denominator from count to differential flux and from differential flux to distribution function, we also show less erroneous differential flux. Even with such large error bar, the data show good match into a smooth curve and good agreement between different spacecraft, giving some reliability in the plot. For example, the positive slope of the electron distribution function at the highest energy is real beyond the possible error bar.

We cannot obtain non-linear term due to the limited quality of the data.

Figure 10b show the result of the decoupling. By using optimum values for the constant (f_1 in the figure), all panels in Fig. 10b show smooth trends that are independent of the Pi2-like magnetic field variation (Figs. 5 and 6). Thus, the decoupling is successful as the first approximation.

The degree of synchronization to the magnetic field variation is roughly represented by the ratio of f_1/f_0 in Fig. 10b. It is large for high energy ($f_1/f_0 > 0.6$ at 240~400 keV) and small for low energy ($f_1/f_0 < 0.4$ at 40~130 keV), i.e., the synchronized modulation is most obvious at the highest energy range. This energy dependency is opposite from the expectation from the conservation of magnetic moment because the $f(W)$ profile in Fig. 11 predicts more obvious in-phase behavior between flux and magnetic field for low energy than for high energy. Therefore, the conservation of the magnetic moment is not the primary cause of the variation of the electron flux synchronized with Pi2-like magnetic field variation.

The same energy dependency of the synchronization with the magnetic field variation is found in the proton flux variation at high energy part (92~160 keV, 160~370 keV, and 370~960 keV) in Fig. 9a. The synchronization is, however, time-delayed: about 20 s delay at 92~160 keV (5000 km/s) channel and about 10 s delay at 160~370 keV (7000 km/s) channel compared to electrons (>10 000 km/s) or 370~960 keV H^+ (10 000 km/s). The time delay again contradicts the conservation of the magnetic moment. In the low energy proton channel (e.g., 75~92 keV), the flux modulation is not synchronized with the magnetic field variation at all. Variation of 75~92 keV proton flux has only one major minimum at around 06:45:30 UT, with SC-2 leading and SC-3 behind by more than 10 s, while magnetic variation near its minimum at around 06:44:55 UT is led by SC-3 and followed by SC-2 in Fig. 6. We could not detect such synchronization for He^+ (Fig. 9b) or O^+ (Fig. 9c), although the velocity of 1 MeV He^+ is the same as that of 250 keV H^+ .

The decoupled plots in Fig. 10b show large-scale trends. The most visible trend is quick decrease of electron fluxes at

Table 2. Gyroradius of major ring current ions under 160 nT magnetic field.

speed	H ⁺	energy He ⁺	O ⁺	H ⁺	gyroradius He ⁺	O ⁺
2000 km/s	21 keV	84 keV	330 keV	130 km	530 km	2100 km
3000 km/s	47 keV	190 keV	750 keV	200 km	800 km	3200 km
4000 km/s	84 keV	330 keV	1.3 MeV	270 km	1100 km	4300 km
5000 km/s	130 keV	520 keV	2.1 MeV	330 km	1300 km	5300 km

all energy ranges and of 160~370 keV proton flux starting at around 06:42:55 UT (same timing as the start of magnetic deviation). The decoupled flux of >240 keV electrons shows its minimum (about 20% decrease) at around 06:44 UT, i.e., when the electric field is strongest (Figs. 5 and 6), and its recovery at around 06:46 UT, i.e., when the electric field changed in both strength and direction. These profiles show good correspondence with electric field.

The recovery of the electron flux is faster at high energy than low energy. Increase of flux at around 06:46 UT is also seen in <64 keV proton and 0.4~0.6 MeV oxygen in Fig. 9a and c. This increase has an upper energy limit in the similar way as the 06:43~06:46 UT event. The flux of 75~160 keV proton decreased and flux of 0.6~0.9 MeV oxygen stayed the same value after 06:46 UT. The similar energy dependency can be recognized for helium. The degree of flux decrease of 140~170 keV helium during 06:46~06:48 UT is not as quick as those for 240~350 keV helium. Thus, the energetic ions show another energy dependent flux change with mass-dependent threshold energy at around 06:46 UT in addition to at around 06:43 UT. The threshold energy (and hence velocity) is different between these two events. In both events, the changes of the fluxes coincide with H⁺ flux increase at 1~10 keV observed by CIS (Fig. 8), electric field change observed by EFW (Fig. 5) and related thermal plasma convection observed by CIS (Fig. 7).

In Fig. 9a, one can recognize another type of inter-spacecraft difference of the flux change at 28~64 keV proton: SC-3 flux stayed the same whereas SC-2 flux showed more than 30% increase (and next energy 75~92 keV shows opposite trend). Since the gyroradius of these energetic ions is larger than the inter-spacecraft distance, this difference suggests either non-gyrotropic behavior or instrumental difference. Solving this question requires solid examination and is beyond the scope of this paper in which we examine large-scale changes.

3.7 Summary of observations

At about 06:43~06:46 UT on 19 May 2002, all Cluster spacecraft observed large DC electric field (up to 10 mV/m), Pi2-like rarefaction of dipole-like magnetic field (decrease up to 25%), convection of He⁺ rich cold ions (up to >50 km/s), sudden arrival of ionospheric ions in the field-aligned direc-

tions, and dual change of energetic ion fluxes without outstanding wave activities. These changes are nearly simultaneous between spacecraft (within 10 s difference between all spacecraft), but did not start until 06:42:50 UT, i.e., they are not parts of global signature of substorm onset, but are signatures of arrival of the auroral bulge.

Due to strong $E \times B$ drift velocity of up to >50 km/s, cold He⁺ and cold H⁺ are detected above 5 eV, while no signature for O⁺ or He⁺⁺ is detected, indicating that the plasmasphere expanded to 4.4 R_E at this time and location. The electric and magnetic field structure was moving sunward, i.e., in the electric field direction with about 5~10 km/s velocity. The total potential drop across the moving structure observed at 06:43~06:46 UT is about 5~10 kV, with the front (sunward) side higher potential than the back (tailward) side.

The changes of energetic ion/electron fluxes are mass-dependent: fluxes of ions with characteristic speed of about 3000 km/s (with upper threshold of about 4500 km/s) increased for all H⁺, He⁺, and O⁺; and fluxes of ions with energy (speed) above or below this energy (speed) decreased. The flux increase is not due to the conservation of the magnetic moment and hence due to net injection. The resultant increase of plasma pressure is comparable to the local decrease of the magnetic pressure at 06:43~06:46 UT. The electron flux of observable energy range (>40 keV) decreased during 06:43~06:46 UT even after removing the synchronizing modulation with the Pi2-like magnetic field variation.

From these observations, we can illustrate the entire picture as Fig. 12. Magnetic drift velocity of 3000 km/s H⁺ is about 10~15 km/s (or about 50 km/s for 3000 km/s He⁺) sunward at this location in the dipole geomagnetic field, and is faster than the propagation velocity of the structure. The different velocities between the propagation, the drift of 3000 km/s H⁺, and the drift of other ions with 3000 km/s speed indicates that the propagation is not due to a simple drift motion of high flux region that is used in the past models (e.g., Vasyliunas, 1970; Wolf, 1970; Wolf and Spiro, 1985; Ebihara, 2009). The energy-time dispersion of H⁺ flux increase is better explained by finite gyroradius effect of dispersion-free increase rather than the time-of-flight effect of energy-dependent drift.

The sudden and nearly simultaneous appearance of the field-aligned H⁺ and O⁺ of about 2~8 keV at around

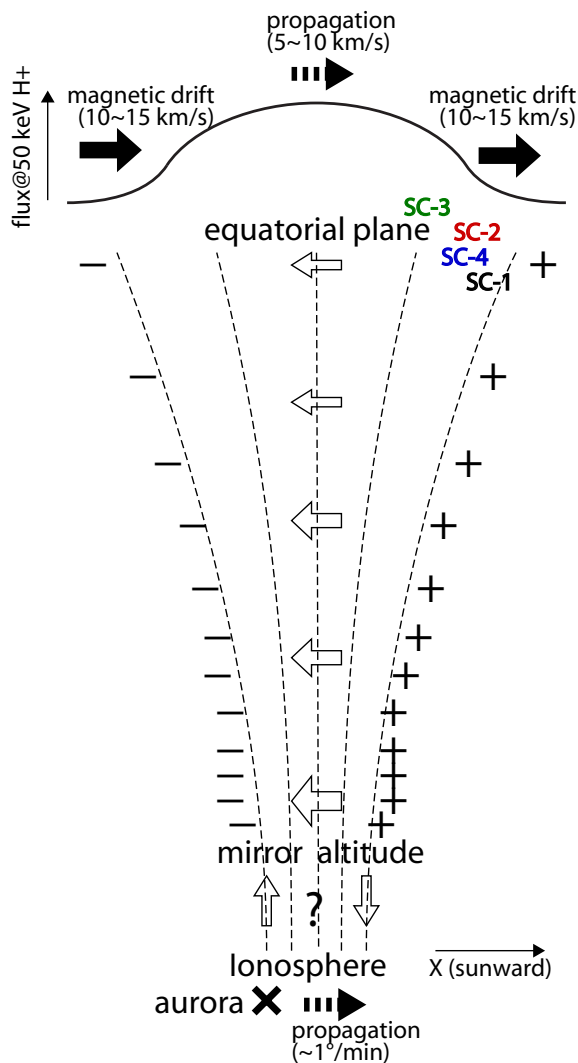


Fig. 12. Schematic illustration of the amplitude of the structure (flux of 3000 km/s ions, strength of electric field, and depletion of the magnetic field) at the top, expected charges (+ and -) along the geomagnetic field (dashed line) and resultant expected electric field (empty arrows) in the middle, and the expected auroral position (cross) at the bottom. The observed propagation velocities (thick dashed arrows) matches between the structure in the magnetosphere and the aurora in the ionosphere. The magnetic (summation of gradient-B and curvature) drift of the 3000 km/s protons is shown by thick arrows. The $E \times B$ drift (30~50 km/s duskward in the magnetosphere) is not illustrated.

06:43:40 UT indicates that Cluster crossed a boundary which is filled with ionospheric ions. These ions are accelerated by the field-aligned potential drop which simultaneously accelerates electron downward to cause the auroral bulge. The direction of the potential drop agrees with the direction of the field-aligned current at the front side of general westward traveling surge.

At the conjugate ionosphere, the westward moving auroral bulge is nearly stagnate after 06:42 UT to $\sim 1^\circ$ longitude/min, which corresponds to a sunward motion of < 10 km/s at the Cluster location. The geomagnetic field at the MCQ station (nearest conjugate) show a sharp change between 06:42 UT and 06:43 UT. Thus, the auroral bulge and the equatorial structure during 06:43~06:46 UT observed by Cluster agree to each other in location, velocity, and the sense of potential drop (upward from ionosphere).

4 Discussion

4.1 Energy modulation by electric field

The observed large gradient of DC electric field might directly modulate the ion flux when the gyroradius is large enough to get ions accelerated or decelerated significantly during the gyromotion. This percentage is proportional to $(\text{mass/energy})^{0.5}$, and hence to velocity^{-1} . Therefore, this finite gyroradius effect causes velocity-dependent flux changes. However, this effect is too small to explain the observed change in Fig. 9. The 10 mV/m electric field and 160 nT magnetic field condition at around 06:44:00 UT means that a 100 keV O^+ and a 6 keV H^+ are accelerated or decelerated by about 10% over the gyroradius distance. A 10% change is large enough to affect CIS observation which has about 25% energy stepping, but not for RAPID energy.

4.2 Primary propagation direction

In Fig. 8, the field-aligned ions of ionospheric origin are observed nearly simultaneously from both summer (northern) ionosphere and from winter (southern) ionosphere. According to Fig. 5, Alfvén velocity during 06:43~06:44 UT is about 200 km/s (slow velocity is mainly due to high density of 300 cm^{-3}), and transit time between both hemispheres is much more than 1 min, far too long to explain the simultaneous change. Although the bouncing signal most likely overlaps with the sunward propagating general structure, such bouncing structure cannot be the cause of the entire structure as described in Sect. 3.2. Particularly, this bouncing scenario cannot explain the selective injection of 3000 km/s ions. Therefore, the primary propagation direction of the observed structure is sunward. In other words, we should consider the sunward propagation as of the entire structure that covers both the magnetosphere and the both ionospheres.

4.3 Diamagnetic current

Depletion of the magnetic field means diamagnetic current in the perpendicular direction to the magnetic field. The sunward propagation of the structure including the front side at around 06:43 UT (start of the sharp decrease of the magnetic field at around 06:43:00 UT is led by SC-3 as described in Sect. 3.2) means a dawnward diamagnetic current at the front

side of the propagation. Then question is the current carrier because the depletion of magnetic pressure is balanced with the local increase of plasma pressure by the injection of 3000 km/s ions (particularly 74~160 keV protons). In such a case of pressure balance, ions that are contributing to the pressure increase are normally the carrier (Alfvén and Fälthammar, 1963). One such example is the solar wind at the magnetopause.

Let us examine the current direction from the gradient of the ion flux. The way of causing the dawnward current is in principle the same as in the magnetopause. Since the gyration velocity of ions with net flux increase (3000 km/s) is much faster than the propagation velocity (5~10 km/s), it is easier to take a rest frame moving with the propagation. In this case, gyromotion of additional ions (of 3000 km/s velocity) is confined to one side. Since extra ions in one side have finite gyroradii of about 200 km for H^+ , the center of the gyromotion of these H^+ must be more than 200 km away from the boundary (propagation front), so that no effect leaks outside this boundary (no signature outside the boundary by definition of the present rest frame). In other words, extra H^+ at the first 200 km from the edge of the boundary must be at the gyration phase pointing one direction (e.g., dawnward for the present case with northward magnetic field and extra ions in the tail side). Such a “surface” flow (200 km wide) of ion points dawnward as long as the flux increase toward the tail. For decreasing flux toward the tail, this surface effect causes a duskward flow.

The same logic works for electrons although the gyroradius is small. The additional electrons mean duskward surface flow and hence the dawnward diamagnetic current in the present case. Thus both ions and electrons has the same surface effect in the direction of the diamagnetic current. In other words, the observed magnetic depletion (dawnward diamagnetic current) is caused by species that show net flux increase. Such a flux increase is seen in only medium energy ions with 3000 km/s speed. The other energies cannot explain the required direction of the diamagnetic current of the propagation. Combined with the quantitative pressure balance, we can safely conclude that the net increase of 3000 km/s ion caused the depletion of the magnetic field except the Pi2-like modulation.

This surface effect has finite width due to the finite gyroradius (200 km for H^+). Due to slow propagation speed (5~10 km/s), it takes 20~40 s until the entire gyration phases of the additional H^+ appear at the same location. This explains slower increase of heavy ions than light ions in Fig. 9 (<1 min for H^+ , 1~2 min for He^+ , and >2 min for O^+).

Unlike the magnetic depletion mentioned above, the Pi2-like magnetic variation is observed simultaneously at all spacecraft. The variation probably represents a wave mode which involves the entire field lines through Alfvén wave or field-line oscillation. For example, bouncing Alfvén wave between the ionosphere and the magnetosphere has been proposed as the cause of the Pi2 pulsation in the westward surging

auroral bulge (e.g., Sato, 1978; Kan and Sun, 1985). However, such pulsation cannot be the cause of the entire structure as mentioned in Sect. 4.2. Rather, the Pi2 like variation is most likely excited by the passage of the sunward propagating structure. This suggests that we need a new model for the generation of the Pi2 pulsation.

4.4 Electric polarization

The alignment between the electric field direction and the propagation direction means an longitudinal electric polarization by the charge separation. Difference between the ion gyroradius and electron gyroradius is often considered as the cause of charge separation when they experience the change in the magnetic field. In the inner magnetosphere, this effect causes the charge separation known as the Alfvén layer (Alfvén and Fälthammar, 1963) although the expected polarization direction is dawn-dusk direction at 19 MLT.

In the present case, the polarization electric field quickly increased from 06:43:25 UT to 06:44:05 UT and quickly decreased from 06:44:10 UT to 06:46:45 UT in Fig. 6. Considering the propagation velocity of 5~10 km/s, the width of the gradient is about 200~400 km for both positive gradient and negative gradient. This matches with gyroradius of 3000 km/s protons, which is about 200 km. Therefore, the finite gyroradius effect of 3000 km/s H^+ is a good candidate for the electric field.

The opposite scenario (electric field maintained by the cold ions/electrons caused the change in the energetic particles) is unlikely because the electric potential of 10 kV is too small to affect the flux of energetic particles. Furthermore, the magnetic field and the electron flux started about 20 s before the change in the electric field or the detection of cold ion convection. Therefore, the electric field is most likely the result of charge separation of the 3000 km/s ions inside the magnetic depletion.

The present type of the propagating charge separation has never been predicted or observed in the evening inner magnetosphere. Propagation of longitudinal polarization is predicted associated with the substorm expansion as a propagation front of magnetosonic compression (Yamauchi et al., 1993; Yamauchi, 1994). However, the present mode keeps pressure balance, which is not satisfied in the magnetosonic compression model.

4.5 Solitary structure maintained by 3000 km/s ions

The magnetic drift of 3000 km/s ions at this location (10~15 km/s for H^+ and 50 km/s for He^+ in the dipole field model) is faster than the propagation velocity of the structure (5~10 km/s). Therefore, these ions overtake the propagating structure as illustrated in Fig. 12. Yet the enhancement of the 3000 km/s ion flux can be maintained as long as the outflow from this structure does not exceed the inflow to this structure from the tail. This semi-trapped view agrees with

the energy-time dispersion of flux increase in Fig. 9, which agrees with finite gyroradius effect of dispersionless increase of flux. Propagation of finite amplitude DC electric and magnetic fields that is maintained by the semi-trapped plasma passing through the structure means that this is a kind of solitary structure. If the influx is larger than outflux, more carriers of diamagnetic current appear inside the structure, enhancing the magnetic depletion. Such influx-outflux unbalance may happen under a new injection, a change of gradient of magnetic field, or an enhancement of duskward electric field.

The magnetic drift theory gives the same drift velocity for different masses for a given energy, and the $\mathbf{E} \times \mathbf{B}$ drift is too small to explain the 3000 km/s velocity. Therefore, the selection of 3000 km/s speed instead of energy has never been predicted inside the magnetosphere. The observed solitary structure is a new finding. We are not able to answer the original cause of selection of 3000 km/s velocity. Inversely, this feature can be one of the key feature in modeling this new type of solitary structure.

The relation between the minor substorm at 06:25 UT and the westward moving auroral bulge is not clear. Geosynchronous LANL-1991 satellite at the same local time as Cluster (about $1.5 R_E$ tailward and $1.9 R_E$ duskward from Cluster in GSE) observed flux increase of 50~500 keV H^+ and flux decrease of 0.1~10 keV H^+ at around 06:37 UT, i.e., 6 min earlier than Cluster. Furthermore, LANL-1994 at earlier local time (about 16LT) observed less intense flux increase of 50~500 keV H^+ at around 06:40 UT with energy-time dispersion. If these flux increases have the same source as the flux increase observed by Cluster, the source of these ions with flux increase is not local and is spreading at wide drift shell. Unfortunately we have no evidence that connect or disconnect observations of LANL and Cluster which are separated about $2 R_E$ in the radial direction.

The propagating magnetospheric solitary structure is not limited to the equatorial plane as illustrated in Fig. 12 because the carrier of the field change is most likely the 3000 km/s particles which can bounce inside the magnetic bottle within tens seconds (a 3000 km/s H^+ travels $4 R_E$ distance in 9 s). Furthermore, a trapped particle spends most of the time near the mirror point rather than the equatorial region (Alfvén and Fälthammar, 1963). Therefore, we expect a larger potential drop across the solitary structure at low altitude than at the equatorial region. This creates large potential drop between the ionosphere and the mirror altitude.

4.6 Effect of $\mathbf{E} \times \mathbf{B}$ drift

The duskward $\mathbf{E} \times \mathbf{B}$ drift speed (up to >50 km/s) is larger than the sunward propagation speed of the solitary structure (5~10 km/s) or the magnetic drift speed of injected ions (30 km/s for 100 keV ions at $L=4.4$). One-minute travel distance of the entire drifting shell of the ring current ions (which is east-west aligned) by the duskward (out-

ward) $\mathbf{E} \times \mathbf{B}$ drift during 06:43:30~06:44:30 UT is about 2500~3000 km (or $0.4\sim0.5 R_E$) for all ions species and energies. This is equivalent to about 1.5° equatorward shift at the ionosphere. From the observational viewpoint, the spacecraft substantially crossed the ring current region about $0.5 R_E$ inward during this one minute (nearly 10 times faster than the spacecraft velocity). However, the observed flux change is not monotonic during 06:43~06:46 UT, indicating that temporal variation is prevailing over the spatial change. Therefore, this does not alter our discussion above. On the other hand, the 1.5° equatorward shift in one minute is important in considering the conjugacy with the ionosphere.

4.7 Relation to the auroral bulge

The solitary structure at 06:43~06:46 UT observed by Cluster agrees with the auroral bulge at 19 MLT in location and velocity, as illustrated in Fig. 12. The direction of the potential drop (upward) observed by Cluster also agrees with auroral electron acceleration downward. Therefore, the auroral bulge is most likely caused by the magnetospheric solitary structure with finite amplitude deviation of DC electric and magnetic fields. The motion of the auroral bulge is the result of the westward propagation of the solitary structure. This possibility has never discussed in the past.

4.8 Plasmaspheric He^+

In Fig. 7 we observed cold He^+ without O^+ or H^{++} ; i.e., we observed the plasmaspheric ions inside the ring current region during a minor storm time. O^+ ions are typically not observed as part of the cold plasmaspheric population, at the Cluster altitudes (Dandouras et al., 2005). The overlap of the plasmasphere with the ring current in the evening sector during a magnetic storm is consistent with the stagnation of eastward drift of the plasmasphere by the storm-time electric field (Chappel, 1972 and references therein) or detached plasmasphere by complicated substorm electric field (Chappel, 1974).

4.9 06:46 UT activity

The strong electric field and the related convection suddenly diminished at around 06:45:55 UT and changed its direction by more than 90° . From field data (Figs. 5 and 6) and auroral ion data (Fig. 8), we concluded that it is a boundary crossing which moved outward. Starting this time, Cluster observed increase in flux for both ions and electrons. The energy range of the flux increase is different from that for the 06:43:00 UT event. During 06:46~06:48 UT, fluxes increased for >240 keV electron, 1~90 keV proton, 240~350 keV helium, and possibly 0.6~0.9 MeV oxygen although the last can be a prolongation of the 06:43 UT event. The flux increase of H^+ is simultaneous for all energies (1~90 keV) without pitch angle-time or energy-time dispersion. The flux increase is predominantly seen in the

perpendicular component to the magnetic field according to the CIS data.

The manner of the flux increase is similar to that during 06:43~06:45 UT, i.e., the characteristic energy of the increasing flux is mass dependent and is related to the sudden change in the DC electric field. The H^+ change took place when the magnetic field is near constant during 06:45:50~06:64:20 UT. Unlike the 06:43 UT event, however, the energy range of the flux increase is very wide, with its low-energy limit for H^+ to extend <1 keV. Even electrons flux increased.

It is quite possible that Cluster observed a stagnant auroral bulge. In this case, the phenomena can be localized to the Cluster location. In fact, LANL-1991 at the same local time did not observe the corresponding second peak when it observed enhancement of 50~500 keV H^+ during 06:37~06:38 UT.

5 Conclusions

We have studied a sudden change in both field and particle starting simultaneously at 06:42:50 UT on 19 May 2002 at all Cluster spacecraft that are located close to the equatorial plane during the event. The event involves both northern and southern ionosphere including auroral bulge, and the entire structure that covers both the magnetosphere and the both ionospheres is moving westward. At equatorial inner magnetosphere, this motion is seen as a 5~10 km/s sunward propagation of the following signatures: (a) sudden rarefaction of equatorial geomagnetic field by 25% together with local diamagnetic current, (b) electric field in the propagation direction up to 10 mV/m, (c) duskward $\mathbf{E} \times \mathbf{B}$ convection of He^+ rich cold plasma without O^+ , up to 50 km/s, (d) flux enhancement of medium energy ring current ions with particle speed of about 3000 km/s for all ion species, which balances with the depletion of the magnetic field in the pressure unit, (e) flux decrease of the other energetic particles beyond the adiabatic invariance can explain, and (f) appearance of the ionospheric plasma that is accelerated by the parallel field-aligned potential which can also accelerate auroral electron.

All these changes are simultaneous at all SC with SC-3 leading by 1~10 s, giving a propagation velocity of 5~10 km/s at $4.4 R_E$, which agrees with westward motion of auroral bulge in the ionosphere ($\sim 1^\circ$ longitude/min). The observations indicate a new type solitary structure in the magnetosphere as the cause of the westward moving auroral bulge:

(1) This solitary structure is composed of polarization electric field in the propagation direction and magnetic depletion, and is maintained by flux enhancement of 3000 km/s ions. Fluxes of the other ring current particles decreased. (2) The structure has about 1000~2000 km width in the propagation direction and propagates sunward with about 5~10 km/s speed. (3) The 3000 km/s ions are the main car-

rier of the propagating diamagnetic current that caused the magnetic depletion propagating sunward. (4) The polarization is maintained by different behaviors between energetic ions and electrons, and particularly the 90~160 keV protons and >240 keV electrons are good candidates for the major charge carriers. (5) The potential drop in the propagation direction (about 5~10 kV tailward at equator) is the ultimate cause of the field-aligned potential drop (several kV upward). (6) The sunward propagation of this solitary structure caused the sunward propagation of field-aligned potential drop and hence of the auroral bulge. (7) The passage of this solitary structure most likely excited the Pi2 like magnetic variation.

The observations also provided new pictures on cold and energetic ions: (8) Plasmasphere expands to the inner magnetosphere where ring current ions are present. We do not know the route of this expansion, though. (9) Pressure-contributing ring current ion flux can be enhanced at certain velocity (3000 km/s in the present case) rather than the same energy for all ion species.

The observation raises a new paradigm on the relation between the ring current and the auroral bulge after substorm: a new type of solitary structure maintained by ring current ions at 3000 km/s speed can be the cause of the westward moving auroral bulge. We certainly need both theoretical and observational effort to understand the solitary structure, its relation to substorms, its relation to pulsation, and selection of the 3000 km/s speed instead of a specific energy.

Acknowledgements. We thank the following organizations and teams for providing the data used in analyses. Geomagnetic indices are provided by WDC-C2 for geomagnetism, Kyoto University. Geomagnetic field data is provided by Geoscience Australia [CSY, MAW, MCQ], Geological Survey of Canada [MEA, PBQ], Danish Meteorological Institute [NAQ], Leirvogur Magnetic Observatory [LRV], Tromsø Geophysical Observatory [BJN], and US Geological Survey [CMO, SIT] through WDC-C2 for geomagnetism. ACE magnetic field data is provided by the ACE/MAG team (PI: N. Ness at Bartol Research Institute) and the ACE Science Center. GOES magnetic field data is provided by GOES magnetic field team (PI: H. Singer at NOAA) and NOAA/GOES project. IMAGE project is supported by NASA. LANL satellite project is managed by Los-Alamos National Laboratory. The Cluster project is managed by ESA. Swedish part of the work is partly supported by Swedish Research Counsel (VR) #621-2005-5005 and #621-2008-3769 and Swedish National Space Board (RS). MY thanks programs for disabled people in Sweden which have made it possible for him to work.

Topical Editor I. A. Daglis thanks T. Lui for his help in evaluating this paper.

References

- Akasofu, S. and Chapman, S.: The ring current, geomagnetic disturbance, and the Van Allen radiation belts, *J. Geophys. Res.*, 66(5), 1321–1350, 1961.

- Akasofu, S.-I., Kimball, D. S., and Meng, C.-I.: The dynamics of the aurora, 2, Westward traveling surges, *J. Atmos. Terr. Phys.*, 27, 173–187, 1965.
- Akasofu, S.-I.: Physics of magnetospheric substorms, *Astrophys. Space Sci. library*, 47, Reidel, 1977.
- Alfvén, H. and Fälthammar, C. G.: *Cosmical Electrodynamics, Fundamental Principles*, Clarendon, Oxford, 1963.
- Arnoldy, R. L. and Chan, K. W.: Particle substorms observed at geostationary orbit, *J. Geophys. Res.*, 74(21), 5019–5028, 1969.
- Balogh, A., Carr, C. M., Acua, M. H., Dunlop, M. W., Beek, T. J., Brown, P., Fornacon, K.-H., Georgescu, E., Glassmeier, K.-H., Harris, J., Musmann, G., Oddy, T., and Schwingenschuh, K.: The Cluster Magnetic Field Investigation: overview of in-flight performance and initial results, *Ann. Geophys.*, 19, 1207–1217, 2001, <http://www.ann-geophys.net/19/1207/2001/>.
- Benediktov, E. A., Getmantsev, G. G., Mityakov, N. A., Papoport, V. O., and Tarasov, A. F.: Relation between geomagnetic activity and the sporadic radio emission recorded by the Elektron satellites, *Kosm. Issled.*, 6, 946–949, 1968.
- Chappel, C. R.: Recent satellite measurements of the morphology and dynamics of the plasmasphere, *Rev. Geophys. Space Phys.*, 10(4), 951–979, 1972.
- Chappel, C. R.: Detached plasma region in the magnetosphere, *J. Geophys. Res.*, 79(13), 1861–1870, 1974.
- Cornilleau-Wehrlin, N., Chauveau, P., Louis, S., Meyer, A., Nappa, J. M., Perraut, S., Rezeau, L., Robert, P., Roux, A., De Villedary, C., De Conchy, Y., Friel, L., Harvey, C. C., Hubert, D., Lacombe, C., Manning, R., Wouters, F., Lefeuvre, F., Parrot, M., Pinon, J. L., Poirier, B., Kofman W., and Louarn, P.: The Cluster spatio-temporal analysis of field fluctuations (STAFF) experiment, *Space Sci. Rev.*, 79, 107–136, doi:10.1023/A:1004979209565, 1997.
- Daglis, I. A.: Ring current dynamics, *Space Sci. Rev.*, 124, 183–202, 2006.
- Dandouras, I., Pierrard, V., Goldstein, J., Vallat, C., Parks, G. K., Rème, H., Gouillart, C., Sevestre, F., McCarthy, M., Kistler, L.M., Klecker, B., Korth, A., Bavassano-Cattaneo, M. B., Escoubet, P., and Masson, A.: Multipoint observations of ionic structures in the plasmasphere by CLUSTER-CIS and comparisons with IMAGE-EUV observations and with model simulations, in: *Inner Magnetosphere Interactions: New Perspectives from Imaging*, Geophysical Monograph, 159, 23–53, AGU, doi:10.1029/159GM03, 2005.
- Décrou, P. M. E., Ferreau, P., Krasnoselskikh, V., Le Guirriec, E., Lévêque, M., Martin, Ph., Randriamboarison, O., Rauch, J. L., Sené, F. X., Séran, H. C., Trotignon, J. G., Canu, P., Cornilleau, N., de Féraudy, H., Alleyne, H., Yearby, K., Mögensen, P. B., Gustafsson, G., André, M., Gurnett, D. C., Darrouzet, F., Lemaire, J., Harvey, C. C., Travnicek, P., and Whisper experimenters: Early results from the Whisper instrument on Cluster: an overview, *Ann. Geophys.*, 19, 1241–1258, 2001, <http://www.ann-geophys.net/19/1241/2001/>.
- Ebihara Y., M.-C. Fok, J. B. Blake, J. F. Fennell: Magnetic coupling of the ring current and the radiation belt, *J. Geophys. Res.*, 113, A07221, doi:10.1029/2008JA013267, 2008.
- Ebihara, Y., Nishitani, N., Kikuchi, T., Ogawa, T., Hosokawa, K., Fok, M.-C., and Thomsen, M. F.: Dynamical property of storm time subauroral rapid flows as a manifestation of complex structures of the plasma pressure in the inner magnetosphere, *J. Geophys. Res.*, 114, A01306, doi:10.1029/2008JA013614, 2009.
- Fujii, R., Hoffman, R. A., Anderson, P. C., Craven, J. D., Sugiura, M., Frank, L. A., and Maynard, N. C.: Electrodynamics parameters in the nighttime sector during auroral substorms, *J. Geophys. Res.*, 99(A4), 6093–6112, 1994.
- Gjerloev, J. W., Hoffman, R. A., Sigwarth, J. B., and Frank, L. A.: Statistical description of the bulge-type auroral substorm in the far ultraviolet, *J. Geophys. Res.*, 112, A07213, doi:10.1029/2006JA012189, 2007.
- Gurnett, D. A.: The Earth as a radio source: Terrestrial kilometric radiation, *J. Geophys. Res.*, 79(28), 4227–4238, 1974.
- Gustafsson, G., André, M., Carozzi, T., Eriksson, A. I., Fälthammar, C.-G., Grard, R., Holmgren, G., Holtet, J. A., Ivchenko, N., Karlsson, T., Khotyaintsev, Y., Klimov, S., Laakso, H., Lindqvist, P.-A., Lybekk, B., Marklund, G., Mozer, F., Mursula, K., Pedersen, A., Popielawska, B., Savin, S., Stasiewicz, K., Tanskanen, P., Vaivads, A., and Wahlund, J.-E.: First results of electric field and density observations by Cluster EFW based on initial months of operation, *Ann. Geophys.*, 19, 1219–1240, 2001, <http://www.ann-geophys.net/19/1219/2001/>.
- Iijima, T. and Potemra, T. A.: The amplitude distribution of field-aligned currents at northern high latitudes observed by Triad, *J. Geophys. Res.*, 81(13), 2165–2174, 1976.
- Inhester, B., Baumjohann, W., Greenwald, R. A., and Nielsen, E.: Joint two-dimensional observations of ground magnetic and ionospheric electric fields associated with auroral zone currents III – Auroral zone currents during the passage of a westward travelling surge, *J. Geophys.*, 49(3), 155–162, 1981.
- Iyemori, T., Takeda, M., Nose, M., Odagi, Y., and Toh, H.: Introduction to mid-latitude geomagnetic indices “ASY” and “SYM” for 2008 (Provisional), WDC-C2 publication, ISSN 0918-5763, available at <http://swdcwww.kugi.kyoto-u.ac.jp/aeasy/asysym2008intro.pdf>, 2009.
- Kamide, Y. and Rostoker, G.: The spatial relationship of field-aligned currents and auroral electrojet to the distribution of night-side auroras, *J. Geophys. Res.*, 82, 5589–5608, 1977.
- Kamide, Y., Sun, W., and Akasofu, S.-I.: The average ionospheric electrodynamics for the different substorm phases, *J. Geophys. Res.*, 101(A1), 99–109, 1996.
- Kamide, Y., Baumjohann, W., Daglis, I. A., Gonzalez, W. D., Grande, M., Joselyn, J. A., McPherron, R. L., Phillips, J. L., Reeves, E. G. D., Rostoker, G., Sharma, A. S., Singer, H. J., Tsurutani, B. T., and Vasyliunas, V. M.: Current understanding of magnetic storms: Storm/substorm relationships, *J. Geophys. Res.*, 103, 17705–17728, 1998.
- Kan, J. R. and Sun, W.: Simulation of the westward traveling surge and Pi 2 pulsations during substorms, *J. Geophys. Res.*, 90(A11), 10911–10922, 1985.
- Lyons, L. R. and Williams, D. J.: Storm-associated variations of equatorially mirroring ring current protons, 1–800 keV, at constant first adiabatic invariant, *J. Geophys. Res.*, 81(1), 216–220, doi:10.1029/JA081i001p00216, 1976.
- Lyons, L. R.: Adiabatic evolution of trapped particle pitch angle distributions during a storm main phase, *J. Geophys. Res.*, 82(16), 2428–2432, doi:10.1029/JA082i016p02428, 1977.
- Lyons, L. R., De la Beaujardiere, O., Rostoker, G., Murphree, S., and Friss-Christensen, E.: Analysis of substorm expansion and surge development, *J. Geophys. Res.*, 95(A7), 10575–10589, 1990.

- Lyons, L. R., Lee, D.-Y., Wang, C.-P., and Mende, S. B.: Global auroral responses to abrupt solar wind changes: Dynamic pressure, substorm, and null events, *J. Geophys. Res.*, 110, A08208, doi:10.1029/2005JA011089, 2005.
- Marklund, G. T.: Auroral phenomena related to intense electric fields observed by the Freja satellite, *Plasma Phys. Control. Fusion*, 39, A195–A226, doi:10.1088/0741-3335/39/5A/020, 1997.
- Maynard, N. C., Burke, W. J., Basinsk, E. M., Erickson, G. M., Hughesa, W. J., Singer, H. J., Yahnin, A. G., Hardy, D. A., and Mozer, F. S.: Dynamics of the inner magnetosphere near times of substorm onsets, *J. Geophys. Res.*, 101(A4), 7705–7736, 1996.
- Mende, S. B., Heeterdicks, H., Frey, H. U., Lampton, M., et al.: Far ultraviolet imaging from the IMAGE spacecraft: 2. Wideband FUV imaging, *Space Sci. Rev.*, 91, 271–285, doi:10.1023/A:1005227915363, 2000.
- Meng, C.-I., Snyder, A. L., and Kroehl, H. W.: Observations of auroral westward traveling surges and electron precipitation, *J. Geophys. Res.*, 83, 575–585, 1978.
- Morioka, A., Miyoshi, Y., Tsuchiya, F., Misawa, H., Yumoto, K., Parks, G. K., Anderson, R. R., Menietti, J. D., and Honary, F.: Vertical evolution of auroral acceleration at substorm onset, *Ann. Geophys.*, 27, 525–535, 2009, <http://www.ann-geophys.net/27/525/2009/>.
- Murphree, J. S. and Cogger, L. L.: Observation of substorm onset, *Proceedings of ICS-1, Kiruna, Sweden, ESA SP, 335*, 207–211, 1992.
- Ober, D. M., Maynard, N. C., Burke, W. J., Peterson, W. K., Sigwarth, J. B., Frank, L. A., Scudder, J. D., Hughes, W. J., and Russell, C. T.: Electrodynamics of the poleward auroral border observed by Polar during a substorm on April 22, 1998, *J. Geophys. Res.*, 106(A4), 5927–5943, 2001.
- Ohtani, S., Nose, M., Rostoker, G., Singer, H., Lui, A. T. Y., and Nakamura, M.: Storm-substorm relationship: Contribution of the tail current to Dst, *J. Geophys. Res.*, 106(A10), 21199–21209, 2001.
- Olson, J. V.: Pi 2 pulsations and substorm onsets: A review, *J. Geophys. Res.*, 104, 17499–17520, 1999.
- Opgenoorth, H. J., Bromage, B., Fontaine, D., La Hoz, C., Huskonek, A., et al.: Coordinated observations with EISCAT and the Viking satellite – The decay of a westward travelling surge, *Ann. Geophys.*, 7(5), 479–499, 1989.
- Pedersen, A., Cattell, C. A., Fälthammar, C.-G., Formisano, V., Lindqvist, P.-A., Mozer, F., and Torbert, R.: Quasistatic electric field measurements with spherical double probes on the GEOS and ISEE satellites, *Space Sci. Rev.*, 37(3–4), 269–312, 1984.
- Reeves, G. D., Fritz, T. A., Cayton, T. E., and Belian, R. D.: Multi-satellite measurements of the substorm injection region, *Geophys. Res. Lett.*, 17(11), 2015–2018, 1990.
- Reeves, G. D. and Henderson, M. G.: The storm-substorm relationship: Ion injections in geosynchronous measurements and composite energetic neutral atom images, *J. Geophys. Res.*, 106(A4), 5833–5844, 2001.
- Reeves, G. D., Henderson, M. G., Skoug, R. M., Thomsen, M. F., Borovsky, J. E., Funsten, H. O., Cson Brandt, P., Mitchell, D. J., Jahn, J.-M., Pollock, C. J., McComas, D. J., and Mende, S. B.: IMAGE, POLAR, and geosynchronous observations of substorm and ring current ion injection, in *Storm-Substorm Relationship*, 91–101, AGU, Washington D.C., 2003.
- Rème, H., Aoustin, C., Bosqued, J. M., Dandouras, I., Lavraud, B., Sauvaud, J. A., Barthe, A., Bouyssou, J., Camus, Th., Coeur-Joly, O., Cros, A., Cuvilo, J., Ducay, F., Garbarowitz, Y., Medale, J. L., Penou, E., Perrier, H., Romefort, D., Rouzard, J., Vallat, C., Alcaydé, D., Jacquey, C., Mazelle, C., d’Uston, C., Möbius, E., Kistler, L. M., Crocker, K., Granoff, M., Mouikis, C., Popecki, M., Vosbury, M., Klecker, B., Hovestadt, D., Kucharek, H., Kuenneth, E., Paschmann, G., Scholer, M., Scokopke, N., Seidenschwang, E., Carlson, C. W., Curtis, D. W., Ingraham, C., Lin, R. P., McFadden, J. P., Parks, G. K., Phan, T., Formisano, V., Amata, E., Bavassano-Cattaneo, M. B., Baldetti, P., Bruno, R., Chionchio, G., Di Lellis, A., Marcucci, M. F., Pallochchia, G., Korth, A., Daly, P. W., Graeve, B., Rosenbauer, H., Vasyliunas, V., McCarthy, M., Wilber, M., Eliasson, L., Lundin, R., Olsen, S., Shelley, E. G., Fuselier, S., Ghielmetti, A. G., Lennartsson, W., Escoubet, C. P., Balsiger, H., Friedel, R., Cao, J.-B., Kovrazhkin, R. A., Papamastorakis, I., Pellat, R., Scudder, J., and Sonnerup, B.: First multispacecraft ion measurements in and near the Earth’s magnetosphere with the identical Cluster ion spectrometry (CIS) experiment, *Ann. Geophys.*, 19, 1303–1354, 2001, <http://www.ann-geophys.net/19/1303/2001/>.
- Rostoker, G.: The polarization characteristics of Pi-2 micropulsations and their relation to the determination of possible source mechanisms for the production of nighttime impulsive micropulsation activity, *Can. J. Phys.*, 45(3), 1319–1335, doi:10.1139/p67-099, 1967.
- Roux, A., Perraut, S., Robert, P., Morane, A., Pedersen, A., Korth, A., Kremser, G., Aparicio, B., Rodgers, D., and Pellinen, R.: Plasma sheet instability related to the westward traveling surge, *J. Geophys. Res.*, 96(A10), 17697–17714, 1991.
- Saito, T., Yumoto, K., and Koyama, Y.: Magnetic pulsation Pi 2 as a sensitive indicator of magnetospheric substorm, *Planet. Space Sci.*, 24, 1025–1029, 1976.
- Sanchez, E. R., Ruohoniemi, J. M., Meng, C.-I., and Friis-Christensen, E.: Toward an observational synthesis of substorm models: Precipitation regions and high-latitude convection reversals observed in the nightside auroral oval by DMSP satellites and HF radars, *J. Geophys. Res.*, 101(A9), 19801–19837, 1996.
- Sato, T.: A theory of quiet auroral arcs, *J. Geophys. Res.*, 83, 1042–1048, 1978.
- Sato, T. and Iijima, T.: Primary sources of large-scale Birkeland current, *Space Sci. Rev.*, 24, 347–366, 1979.
- Shiokawa, K., Yumoto, K., and Olson, J. V.: Multiple auroral brightenings and associated Pi 2 pulsations, *Geophys. Res. Lett.*, 29(11), 1537, doi:10.1029/2001GL014583, 2002.
- Vasyliunas, V. M.: Mathematical models of magnetospheric convection and its coupling to the ionosphere, in *Particles and Fields in the Magnetosphere*, edited by B. McCormac, pp. 60–71, D. Reidel, Norwell, Mass., 1970.
- Weimer, D. R., Craven, J. D., Frank, L. A., Hanson, W. B., Maynard, N. C., Hoffman, R. A., and Slavin, J. A.: Satellite measurements through the center of a substorm surge, *J. Geophys. Res.*, 99(A12), 23639–23649, 1994.
- Wilken, B., Daly, P. W., Mall, U., Aarsnes, K., Baker, D. N., Belian, R. D., Blake, J. B., Borg, H., Büchner, J., Carter, M., Fennell, J. F., Friedel, R., Fritz, T. A., Gliem, F., Grande, M., Kecskemety, K., Kettmann, G., Korth, A., Livi, S., McKenna-Lawlor, S., Mursula, K., Nikutowski, B., Perry, C. H., Pu, Z. Y., Roeder, J., Reeves, G. D., Sarris, E. T., Sandahl, I., Sraas, F., Woch, J., and Zong, Q.-G.: First results from the RAPID imaging ener-

- getic particle spectrometer on board Cluster, *Ann. Geophys.*, 19, 1355–1366, 2001, <http://www.ann-geophys.net/19/1355/2001/>.
- Williams, D. J.: Dynamics of the Earth's ring current, *Space Sci. Rev.*, 42, 375–396, 1985.
- Williams, D. J.: Ring current and radiation belts, *Rev. Geophys.*, 25, 570–578, 1987.
- Wolf, R. A.: Effects of ionospheric conductivity on convection flow of plasma in the magnetosphere, *J. Geophys. Res.*, 75(25), 4677–4698, doi:10.1029/JA075i025p04677, 1970.
- Wolf, R. A. and Spiro, R. W.: Particle behavior in the magnetosphere, in: *Computer Simulation of Space Plasma*, edited by: H. Matsumoto and T. Sato, pp. 227–254, D. Reidel, Hingham, Mass., 1985.
- Yamauchi, M., Lundin, R., and Lui, A. T. Y.: Vorticity equation for MHD fast waves in geospace environment, *J. Geophys. Res.*, 98, 13523–13528, 1993.
- Yamauchi, M.: Numerical simulation of large-scale field-aligned current generation from finite-amplitude magnetosonic waves, *Geophys. Res. Lett.*, 21, 851–854, 1994.
- Yamauchi, M., Iyemori, T., Frey, H., and Henderson, M.: Unusually quick development of a 4000 nT substorm during the initial 10 min of the 29 October 2003 magnetic storm, *J. Geophys. Res.*, 111, A04217, doi:10.1029/2005JA011285, 2006.